forests

MDPI

Article

Wildfire Susceptibility Mapping Using Deep Learning Algorithms in Two Satellite Imagery Dataset

Nazanin Bahadori [1], Seyed Vahid Razavi-Termeh [2], Abolghasem Sadeghi-Niaraki [2,*], Khalifa M. Al-Kindi [3], Tamer Abuhmed [4], Behrokh Nazeri [5] and Soo-Mi Choi [2]

[1] Geoinformation Technology Center of Excellence, Faculty of Geodesy & Geomatics Engineering, K.N. Toosi University of Technology, Tehran 163171419, Iran; nazibhd4@gmail.com
[2] Department of Computer Science & Engineering and Convergence Engineering for Intelligent Drone, XR Research Center, Sejong University, Seoul 05006, Republic of Korea; razavi@sejong.ac.kr (S.V.R.-T.); smchoi@sejong.ac.kr (S.-M.C.)
[3] UNESCO Aflaj Studies, Archaeohydrology, University of Nizwa, Nizwa 616, Oman; alkindi.k@unizwa.edu.om
[4] College of Computing and Informatics, Sungkyunkwan University, Suwon 16419, Republic of Korea; tamer@skku.edu
[5] Lyles School of Civil Engineering, Purdue University, West Lafayette, IN 47907, USA; bnazeri@purdue.edu
* Correspondence: a.sadeghi@sejong.ac.kr

Abstract: Recurring wildfires pose a critical global issue as they undermine social and economic stability and jeopardize human lives. To effectively manage disasters and bolster community resilience, the development of wildfire susceptibility maps (WFSMs) has emerged as a crucial undertaking in recent years. In this research endeavor, two deep learning algorithms were leveraged to generate WFSMs using two distinct remote sensing datasets. Specifically, the Moderate-Resolution Imaging Spectroradiometer (MODIS) and Landsat-8 images were utilized to monitor wildfires that transpired during the year 2021. To develop an effective WFSM, two datasets were created by incorporating 599 wildfire locations with Landsat-8 images and 232 sites with MODIS images, as well as twelve factors influencing wildfires. Deep learning algorithms, namely the long short-term memory (LSTM) and recurrent neural network (RNN), were utilized to model wildfire susceptibility using the two datasets. Subsequently, four WFSMs were generated using the LSTM (MODIS), LSTM (Landsat-8), RNN (MODIS), and RNN (Landsat-8) algorithms. The evaluation of the WFSMs was performed using the area under the receiver operating characteristic (ROC) curve (AUC) index. The results revealed that the RNN (MODIS) (AUC = 0.971), RNN (Landsat-8) (AUC = 0.966), LSTM (MODIS) (AUC = 0.964), and LSTM (Landsat-8) (AUC = 0.941) algorithms demonstrated the highest modeling accuracy, respectively. Moreover, the Gini index was employed to assess the impact of the twelve factors on wildfires in the study area. The results of the random forest (RF) algorithm indicated that temperature, wind speed, slope, and topographic wetness index (TWI) parameters had a significant effect on wildfires in the study region. These findings are instrumental in facilitating efficient wildfire management and enhancing community resilience against the detrimental effects of wildfires.

Keywords: wildfire; satellite imagery; spatial modeling; deep learning algorithms

Citation: Bahadori, N.; Razavi-Termeh, S.V.; Sadeghi-Niaraki, A.; Al-Kindi, K.M.; Abuhmed, T.; Nazeri, B.; Choi, S.-M. Wildfire Susceptibility Mapping Using Deep Learning Algorithms in Two Satellite Imagery Dataset. *Forests* **2023**, *14*, 1325. https://doi.org/10.3390/f14071325

Academic Editors: Paul Sestras, Ștefan Bilașco, Mihai Nita and Sanda Roșca

Received: 18 May 2023
Revised: 23 June 2023
Accepted: 24 June 2023
Published: 28 June 2023

1. Introduction

Forests support diverse ecosystems and significantly affect human and animal populations. Forests cover nearly 29% of the Earth's surface and are integral to various aspects of our lives and the environment [1]. However, wildfires present a substantial challenge, as approximately 3% of forests experience these events each year [1]. The consequences of wildfires extend beyond immediate damage, leading to long-term environmental impacts and posing threats to both human and animal well-being.

Wildfires bring about ecological disturbances, such as soil erosion, alterations in water hydrology, increased greenhouse gas emissions, and global warming [2–5]. These effects can undermine the stability of ecosystems and hinder the provision of vital resources that contribute to human welfare [2–5].

Iran falls within a subtropical zone of high atmospheric pressure in the earth's arid belt, rendering it prone to wildfires due to warm winds, lightning, and inadequate precipitation [6]. According to the Natural Resources and Watershed Management Organization of Iran, the Zagros Mountain range is the country's largest forest, covering five million hectares, with oak as the dominant species, accounting for 40% of all forests in Iran [7,8]. The Zagros forests are also susceptible to fires caused by wood smuggling, tribal conflicts, and uncontrolled fires by tourists.

Additionally, it is worth noting that due to these factors, Zagros forests are particularly prone to fire outbreaks, with several instances of severe fires having occurred in recent years, causing significant ecological and economic damage. Controlling wildfires requires pinpointing their causes and identifying the areas most susceptible to them [9]. Topography and climate play a significant role in the growth and spread of wildfires [10], and timely intervention is critical when regional conditions favor their spread [11]. However, achieving such control using on-ground methods and human resources over large forest areas is not economical. Initially, sensor-based detection systems were used to identify wildfires [12–14]. However, installing these systems in open spaces is expensive and can be hampered by environmental factors such as infrared or ultraviolet interference and short-range detection distance [15,16].

In recent years, remote sensing (RS) technology has been widely used for monitoring wildfires due to the accessibility, high temporal-spatial resolution, and multispectral nature of RS data [17–20]. The use of satellite images and RS technology has proven effective in detecting and monitoring wildfire behavior and dynamics, enabling more precise data and saving time and human resources [21,22]. Thus, satellite images and RS technology are crucial tools for preventing the spread of wildfires and monitoring them on a large scale and in real-time. Various satellite images have been employed in previous studies to monitor and manage wildfires. For instance, Jaiswal et al. (2002) used the Indian Remote Sensing Satellite (IRSS) and fire risk index to identify burnt areas [23], while Erten et al. (2004) employed Thematic Mapper (TM) images of the Landsat satellite for the same purpose [24]. Awang and Pradham (2006) used the Advanced Very High-Resolution Radiometer (AVHRR) data of the National Oceanic and Atmospheric Administration (NOAA) satellite and Enhanced Thematic Mapper (ETM) images of Landsat-7 to identify areas vulnerable to wildfire. Similarly [25], Schroeder et al. (2016) identified wildfires using Landsat-8 by determining the thresholds of thermal and spectral bands [26]. Zhang et al. (2017) used a set of Visible Infrared Imaging Radiometer Suite (VIIRS) data to identify active wildfires [27], and Gargiulo et al. (2019) employed the Sentinel-2 images and Convolutional Neural Network (CNN) algorithm to identify active wildfires [28]. Finally, Konkathi and Shetty (2021) used the Landsat-8 Operational Land imager (OLI) and Sentinel-2 images to identify burnt areas [29].

Various target mapping methods have been used in fire monitoring research. Among the target mapping methods used in wildfire monitoring, Change Detection [30], the use of hyperspectral image analysis and dimension reduction [31,32], the use of spectral indices such as NBR (Normalized Burn Ratio) and NDVI (Normalized Difference Vegetation Index) [33], and the utilization of thermal data [34] can be mentioned.

Geographical technologies such as RS and geographical information systems (GIS) play a crucial role in wildfire detection and the preparation of wildfire susceptibility maps. These maps provide essential information for evaluating conditions and making decisions regarding wildfires. However, simulating and analyzing wildfire behavior using parameters collected from the field can be challenging. To overcome this challenge, models, maps, and databases in GIS are employed in simulating wildfires [33]. Wildfire susceptibility maps (WFSM) can be created using either knowledge-based or data-driven

techniques. Knowledge-based techniques require expert analysis to identify factors that influence the data processing and implement the models. Examples of knowledge-based techniques include the technique for order preference by similarity to ideal solution (TOPSIS) [35], VIekriterijumsko KOmpromisno Rangiranje (VIKOR) [36], analytic hierarchy process (AHP) [37], and weighted linear combination (WLC) [38]. However, these techniques are prone to human errors and lack sensitivity to outlier data, which can lead to reduced accuracy [39].

Data-driven techniques can be either statistical or artificial intelligence methods. Statistical methods such as the weight of the evidence (WOE) [40,41], frequency ratio (FR) [41,42], and evidential belief function (EBF) [43] assume that the relationships between influential factors in wildfires remain the same in the past and future. However, the complex and nonlinear interaction between environmental factors, such as climate and topography, can limit the accuracy of these methods [44–46].

To address these limitations, researchers have turned to machine learning as an alternative. Machine learning algorithms have a data-driven approach that can handle large-scale nonlinear data and process it quickly. Multiple linear regression (MLR) [47], logistic regression (LR) [48], random forest (RF) [49], bagging (BA) [50], decision tree (DT) [51,52], AdaBoost [53] adaptive neuro-fuzzy interface system (ANFIS) [54], support vector machine (SVM) [55], and artificial neural network (ANN) [56] are all examples of machine learning techniques that have been used to create WFSM.

These techniques have successfully solved complex relationships caused by the interaction and dependence of explanatory variables [44,57–62]. Machine learning plays a crucial role in feature extraction, which can be a challenging task when dealing with a vast amount of data. Studies have found that training machine learning algorithms on large datasets can lead to a decrease in their accuracy, ultimately limiting their ability to extract features at higher levels and handle complex problems effectively [63].

However, combining multiple processing layers can improve feature extraction [64]. Unlike traditional methods that require expert skills, machine learning-based feature extraction requires only simple preprocessing, and the algorithm can automatically learn features from the data [65]. Deep learning using deep neural networks has been shown to produce more accurate results due to the presence of multiple hidden layers [66,67]. Convolutional Neural Networks (CNNs), Recurrent Neural Networks (RNNs), Long Short-Term Memory (LSTM) networks, Generative Adversarial Networks (GANs), Radial Basis Function networks (RBFs), and Deep Belief Networks (DBNs) are among the deep learning algorithms that are composed of layers, learnable parameters, and error functions [68]. Due to their structure, CNNs are widely used in image recognition and description. Therefore, convolutional neural networks are extensively employed in applications such as face recognition and computer vision [69]. In addition, recurrent neural networks play a significant role in analyzing sequential data, which greatly benefits tasks such as speech recognition and control systems [70,71].

Wildfire risk monitoring and mapping have been achieved using deep learning techniques such as CNN [72,73], RNN [74], and LSTM [75]. For instance, Zhang et al. (2019) used CNN to predict the spatial distribution of wildfires in Yunnan Province, China [76], while Ngo et al. (2021) employed RNN and CNN to identify burnt areas on a national scale in Iran [74]. Xingdong et al. (2021) utilized LSTM and drone images to predict the propagation rate of wildfires [77]. Data-driven models are often selected empirically through trial and error due to the differences in conditions and influential factors in various regions [50]. In this study, two deep learning algorithms, RNN and LSTM, were used to prepare wildfire susceptibility maps using Landsat-8 and MODIS satellite images, which is an innovative approach. This study focused on modeling wildfire susceptibility by comparing two remote sensing datasets, MODIS and Landsat-8. The innovative aspect lies in evaluating these datasets using two deep learning algorithms—RNN and LSTM. The research aimed to determine the most suitable remote sensing dataset for fire susceptibility modeling. The primary contribution of this research is evaluating the dataset's performance and the effec-

tiveness of the deep learning algorithms in capturing and predicting wildfire susceptibility. Through performance assessment, the study provided insights into the strengths and limitations of the analyzed datasets and deep learning algorithms. This research improves wildfire modeling by exploring data sources and deep learning techniques.

2. Materials and Methods

2.1. Methodology

The present study aimed to detect and map wildfire susceptibility by following a four-step methodology, which involved data collection, preprocessing, modeling using deep learning algorithms, and evaluating the accuracy of wildfire susceptibility maps.

In the first step, satellite images obtained from Landsat-8 and MODIS were utilized to monitor wildfire areas. These images provided essential information on the characteristics and condition of forest areas, thereby enabling the identification of potential fire-prone zones.

In the second step, the collected data underwent extensive preprocessing through various statistical analyses. For instance, the multicollinearity test was conducted to examine the correlation among predictor variables, while the RF method and Gini index were employed to evaluate the significance of the criteria. These analyses aimed to ensure the accuracy and reliability of the data before modeling.

The third step involved modeling the wildfire susceptibility maps using two deep learning algorithms, namely RNN and LSTM, and the two aforementioned datasets. These algorithms were selected based on their superior performance in handling large and complex datasets. By combining the two datasets and the algorithms, the present study aimed to achieve a more accurate prediction of wildfire susceptibility.

Finally, the accuracy of the wildfire susceptibility maps was evaluated in the last step. The mean square error (MSE) index and the receiver operating characteristic (ROC) curve were used for this purpose. The MSE index provided an assessment of the overall accuracy of the model, while the ROC curve evaluated the performance of the model in terms of sensitivity and specificity.

In summary, the present study adopted a rigorous and comprehensive methodology that involved multiple steps to detect and map wildfire susceptibility. Figure 1 provides a visual representation of the methodology followed in this study.

2.2. Study Area

Gachsaran County is located in the Kohgiluyeh and Boyer-Ahmad Province in Western Iran (Figure 2). As one of Iran's most critical forest areas, it is located in the Zagros Mountains range at the height of 113–3177 m above mean sea level. The county has an area of 3929 km^2, of which 70% is occupied by 320,000 pastureland and 115,000 hectares of forests. Of the forests and meadows of different county areas, a total of approximately 900 hectares experienced significant damages in the year 2021.

Located in a tropical region, Gachsaran has a dry tropical climate in the east and a dry climate in the west. The county has a temperature of 30–40 °C and a mean annual precipitation of 6.5–30.13 mm. Performed evaluations indicate land use and climate change as the major factors responsible for the wildfires in the forests of Gachsaran [78].

2.3. Data

2.3.1. Previous Wildfires

In the present study, the images of Landsat-8 OLI/TIRS and MODIS in the Google Earth Engine (GEE) on May 20, July 8, and October 9, 2021, were employed to monitor the areas burnt due to wildfires in Gachsaran County. Cloud filtering in the GEE was employed on images with a threshold limit of lower than ten. The normalized burn ratio (NBR) was used to identify burnt areas [79] on the images of the MODIS and Landsat-8 satellites. Previous studies have shown that spectral indices derived from time-series images are highly effective in identifying burned areas. These indices are obtained using spectral

analysis techniques. The NBR spectral index combines data from visible to shortwave-infrared spectral bands, which capture color variations, soil composition, moisture, plant chlorophyll, and more. By extracting features from both healthy and burned vegetation, it facilitates the accurate identification of wildfire-affected areas [80]. The NBR index is calculated using Formula (1).

$$\mathrm{NBR} = \frac{\mathrm{SWIR} - \mathrm{NIR}}{\mathrm{SWIR} + \mathrm{NIR}} \quad (1)$$

NBR values higher than one indicate intact vegetation. Areas with NBR values close to zero are considered not burnt, and negative NBR values indicate recently burnt areas.

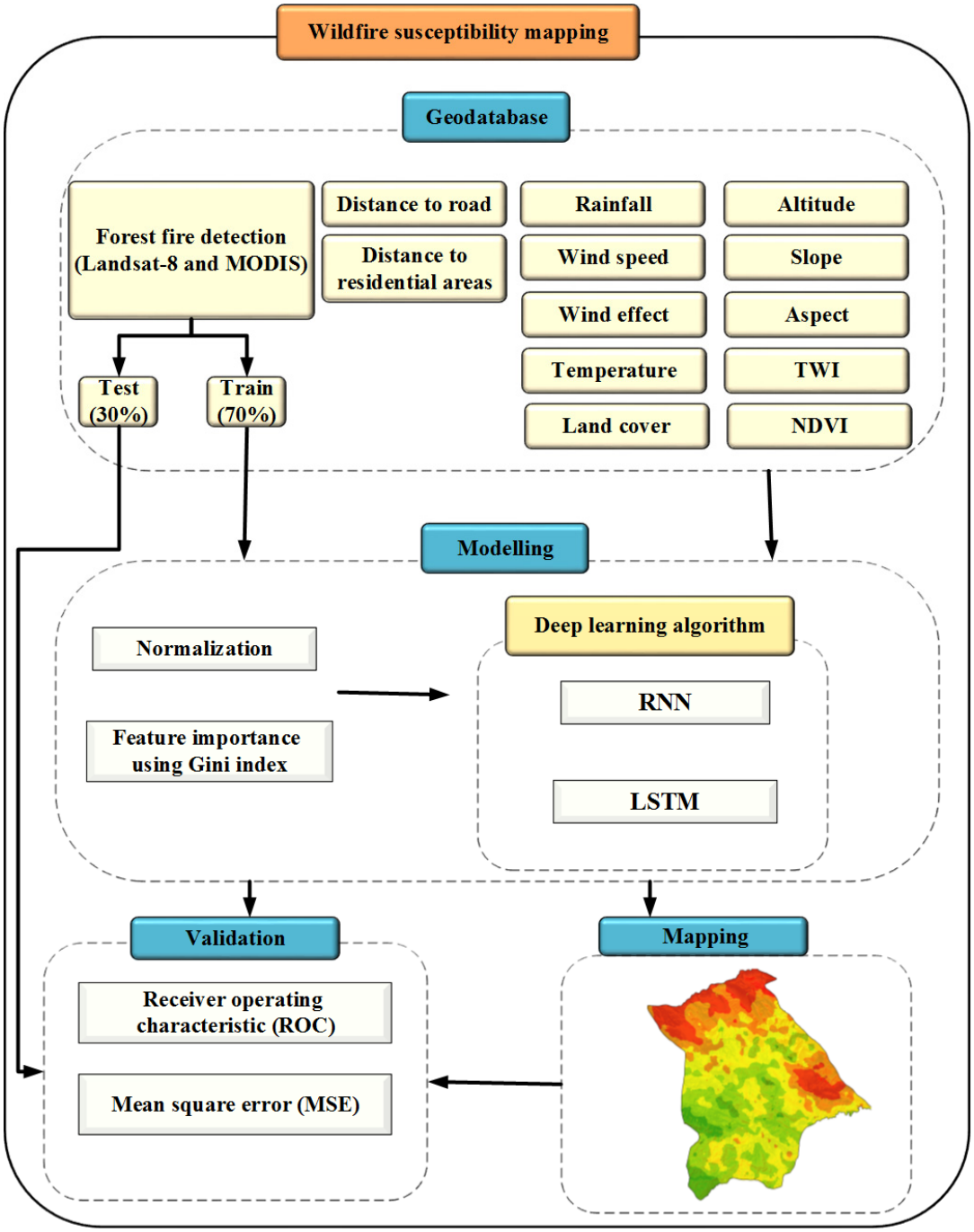

Figure 1. Workflow of the study.

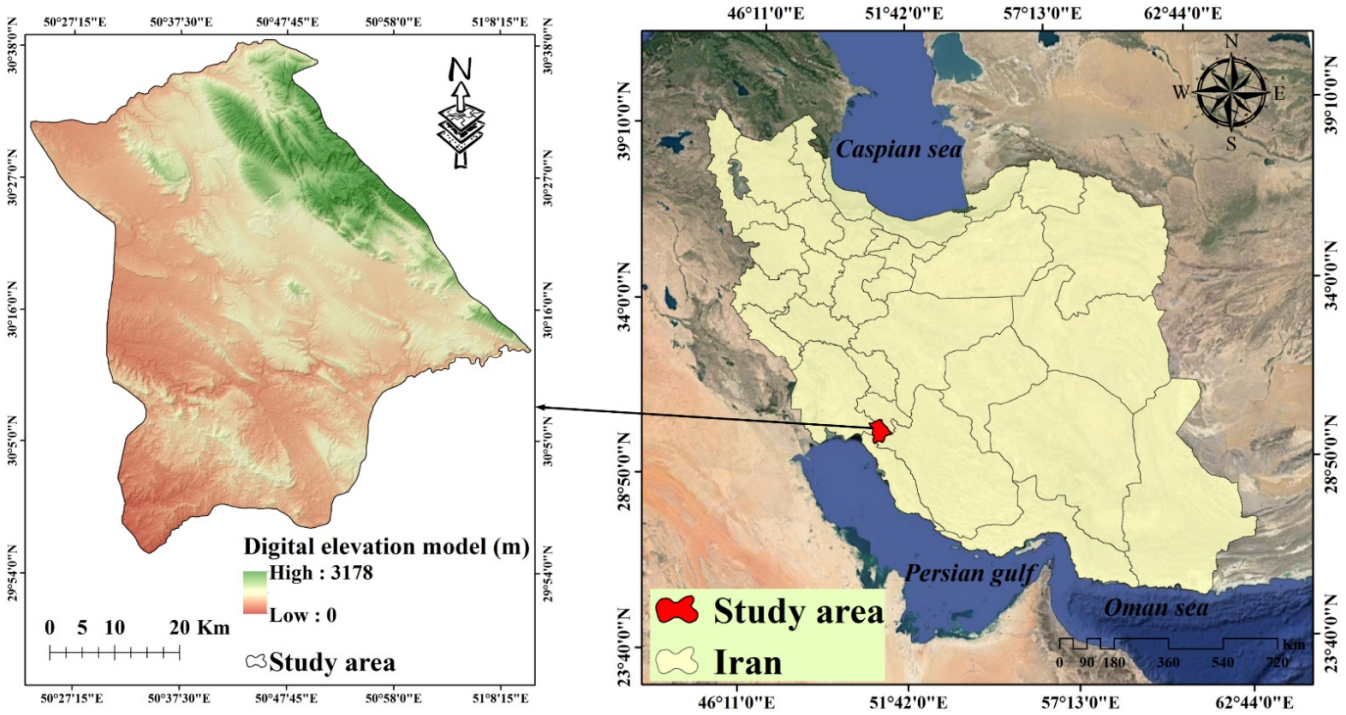

Figure 2. Geographical location of the study area in the country.

By calculating the difference between the post-fire Normalized Burn Ratio (NBRpost) and the pre-fire Normalized Burn Ratio (NBRpre), valuable information can be obtained for the identification of burnt regions. This calculation can be represented according to Equation (2): [81].

$$dNBR = NBRpre - NBRpost, \quad (2)$$

The images of Landsat-8, produced by the United States Geological Survey (USGS) (https://www.usgs.gov/) (20 May 2021), consist of five visible and near-infrared (VNIR) bands and two short-wave infrared (SWIR) bands. To apply the NBR index in Landsat-8, bands B5 and B7, VNIR, and SWIR bands of Landsat-8 were used according to Equation (1). In the two-band spectrum, the chlorophyll content of vegetation is reflected, while in the 5-band spectrum, the presence of water affects the reflection of vegetation. Since the quality of vegetation coverage depends on these two factors, it can be used to assess the intensity of vegetation burning [82].

The burnt areas caused by wildfires were monitored using the "MCD43A4 V6" dataset of MODIS. The data of the MODIS satellites are updated every 16 days. This dataset has high accuracy and resolution due to combining the data of both Terra and Aqua spacecraft and choosing the best representative pixels among the two. In this Equation, NIR indicates Nadir_Reflectance_Band2, and SWIR indicates Nadir_Reflectance_Band7 of MODIS images.

The areas of wildfires using two remote sensing datasets by dNBR index are shown in Figure 3. After identifying the burned areas using satellite images, the affected areas are quantitatively analyzed in ArcGIS 10.6 software (ESRI, Redlands, CA, USA, http://www.esri.com (20 May 2021)), where they are converted into a series of points. In Landsat 8, a total of 599 points are designated as occurrence points, indicating areas that have been affected by fire. Similarly, in MODIS, 232 points were identified as occurrence points, representing regions impacted by fire. These occurrence points are labeled as target 1 in the supervised learning (deep learning) modeling approach used. Since supervised learning (deep learning) is used for modeling, an equal number of non-occurrence points (areas that have not been affected by fire) is required. The same number of points were randomly selected as non-occurrence points in unaffected areas to improve the performance

of deep learning models, and a target value of 0 was assigned to these points. To evaluate the accuracy of the proposed models, 70% of the data were used for training and 30% were used for testing purposes Figure 4.

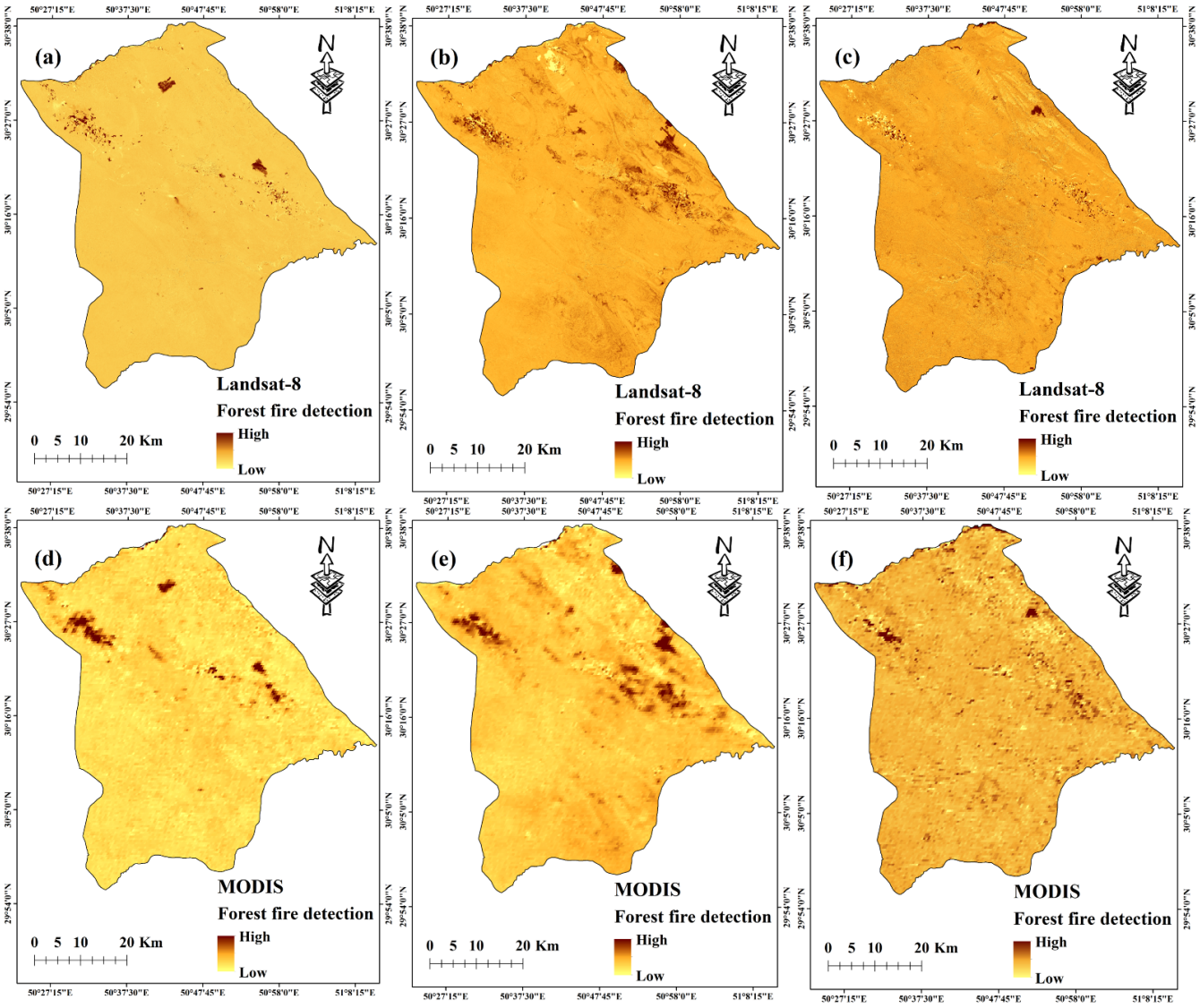

Figure 3. Wildfire detection in two remote sensing datasets by dNBR index: (**a**) Landsat-8 (20 May 2021); (**b**) Landsat-8 (8 July 2021); (**c**) Landsat-8 (9 October 2021); (**d**) MODIS (20 May 2021); (**e**) MODIS (8 July 2021); (**f**) MODIS (9 October 2021).

2.3.2. Effective Factors

In order to develop accurate predictor models for wildfires, it is important to carefully consider the influential factors that contribute to their occurrence and propagation. These factors can be broadly categorized into four main groups: topographic, climatic, human-caused, and vegetation factors [76,83–88]. The selection of these factors is crucial, as they play a significant role in determining the accuracy and reliability of the predictor models [43,85,89–91].

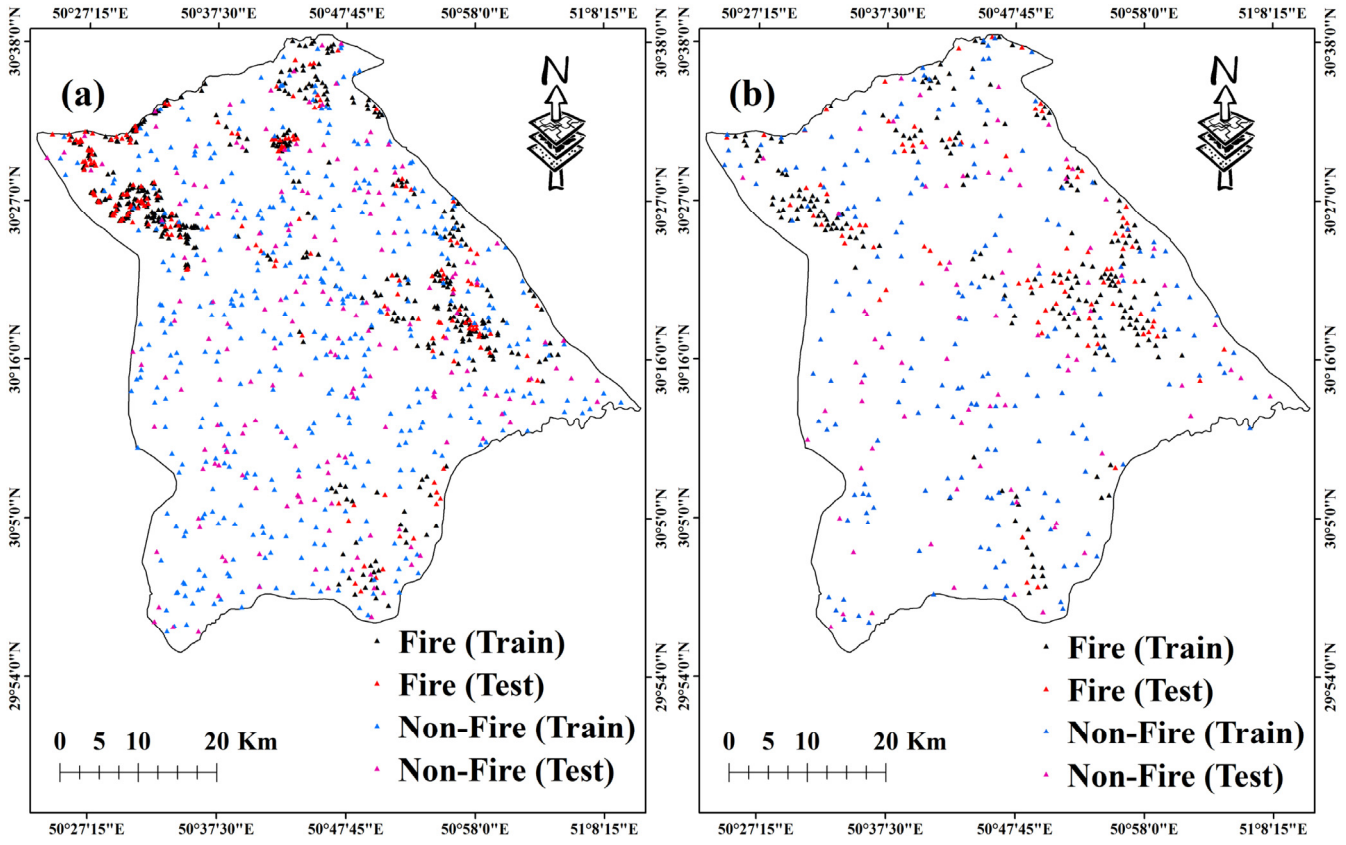

Figure 4. Wildfire occurrence points by two remote sensing datasets: (**a**) Landsat-8 and (**b**) MODIS.

In accordance with previous studies [92–97] and the availability of data, four criteria were selected for the present study. These criteria include climatic factors such as temperature, rainfall, wind speed, and wind effect, topographic factors such as altitude, slope, slope aspect, and topographic wetness index (TWI), human-caused factors such as distance from roads and distance from residential areas, and vegetation factors such as land cover and normalized difference vegetation index (NDVI). A graphical representation of these criteria is provided in Figure 5. Topography is an important factor in evaluating wildfires [6,90]. Altitude, slope, slope aspect, and TWI are topographic parameters that have been shown to influence fire behavior [43,98,99]. Altitude affects vegetation and ground evapotranspiration through its relationship with the temperature of the ground surface, which plays a critical role in wildfire susceptibility [100,101]. Slope angle is another essential factor that influences the propagation of wildfires. The speed of wildfire propagation increases with the slope angle [102]. Slope aspect affects solar radiation and moisture in the region [103]. Studies on the effects of slope aspect on wildfire propagation have shown that south-facing slopes in the northern hemisphere, along with east-facing slopes, receive more light, resulting in lower moisture, drier vegetation, and increased wildfires [104,105]. The topographic criteria were developed using a digital elevation model (DEM) prepared from Shuttle Radar Topography Mission (SRTM) images in ArcGIS 10.6 software to ensure the accuracy of the data. Moisture is inversely related to the wildfire probability and height [106]. As in previous studies, the TWI was used to measure and evaluate this factor [107]. Higher values of TWI indicate higher moisture in a region, resulting in increased NDVI and reduced propagation of wildfires [103]. The TWI was developed in the SAGA GIS 8.2.1 software (Equation (3)).

$$\mathrm{TWI} = ln\left(\frac{\alpha}{\tan\beta}\right) \quad (3)$$

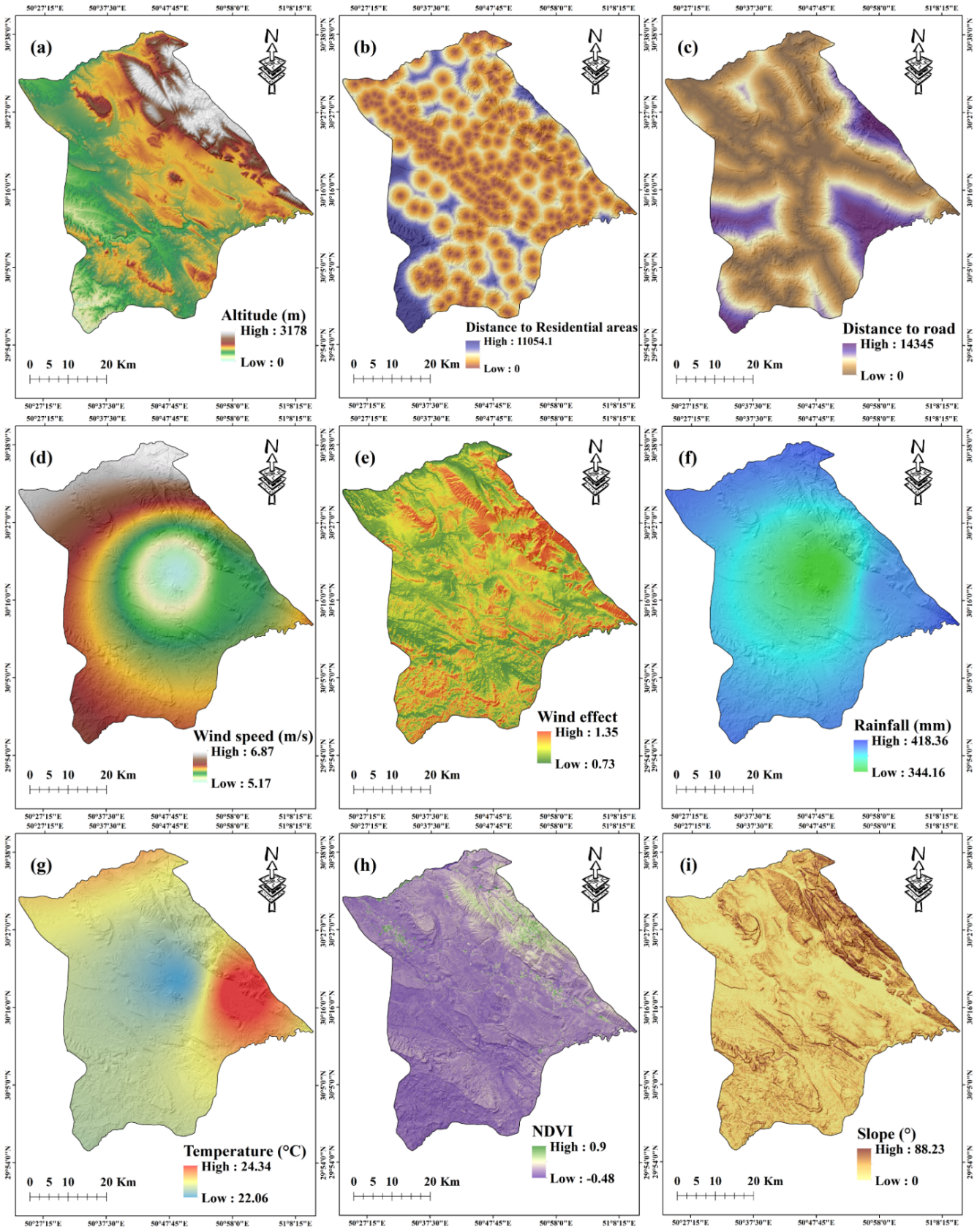

Figure 5. *Cont.*

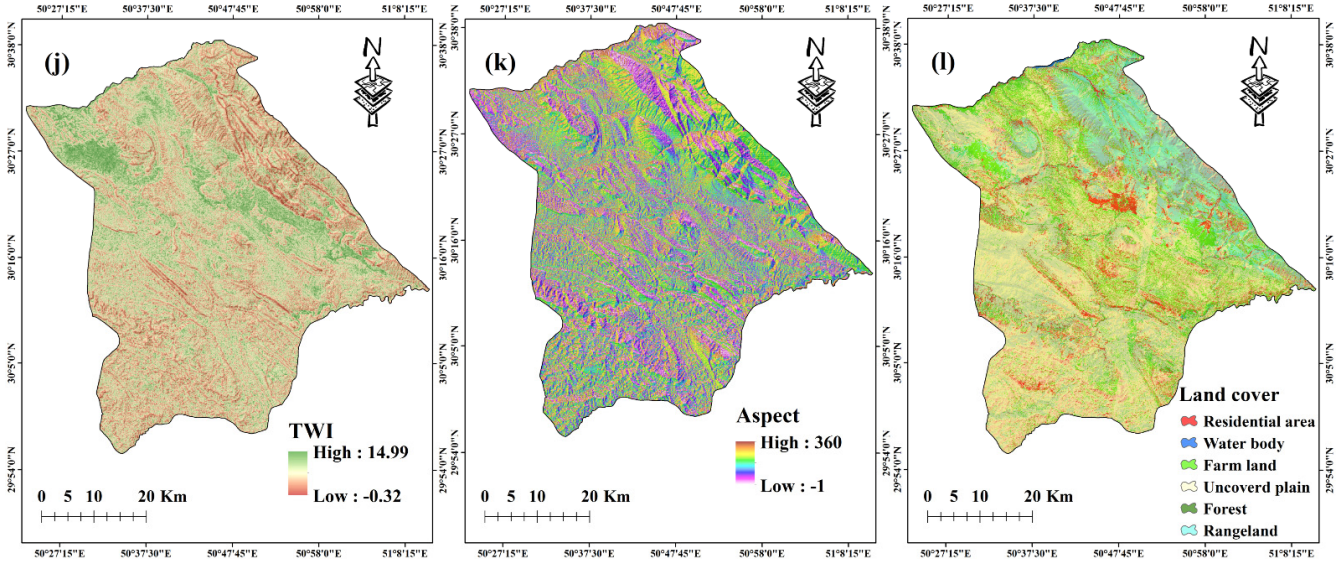

Figure 5. Wildfire influential factors: (**a**) altitude; (**b**) distance to residential areas; (**c**) distance to road; (**d**) wind speed; (**e**) wind effect; (**f**) rainfall; (**g**) temperature; (**h**) NDVI; (**i**) slope; (**j**) TWI; (**k**) aspect; and (**l**) land cover.

α is the area of the basin, and tan(β) is the slope angle at that point.

The temperature, wind, and rainfall are among the essential climatic factors responsible for wildfires occurring in warm, dry, and windy conditions of forests [100,108]. Given the direct impact of temperature on air and soil moisture, it also has a controlling role in the fuel's moisture [109].

High temperatures and low precipitation increase the risk of wildfires in forests [110,111]. The rise in rainfall increases the soil's moisture, resulting in an area's increased moist vegetation. These two factors limit wildfires [112]. To calculate the spatial distribution of climate criteria, the mean temperature, wind speed, and annual rainfall data were collected from five meteorological stations in the studied area from 2011 to 2021. Then, the criteria map was prepared using the inverse distance weighted (IDW) interpolation method and the 30 × 30 m spatial resolution in the ArcGIS 10.6 software.

Given its crucial role in vegetation, moisture, and soil topography, wind speed influences wildfires [113,114]. Wind speed is another influential factor in the propagation of wildfires since the orientation of wildfires is significantly impacted by it [115,116]. The wind direction and speed data were derived from a 10-year climatic dataset based on the weather stations in the Kohgiluyeh and Boyer-Ahmad province. The wind effect criterion was also prepared using the three factors of wind direction, wind speed, and DEM of the studied area in the SAGA-GIS 8.2.1 software [117].

Human activities such as hunting, illegal logging, picnics, and smoking are among the main causes of wildfires [118–122]. Previous studies have shown that the distance from roads and residential areas are important human-caused factors in wildfires [10,121–125]. Roads are a key link between human activities and forests, and short distances from residential areas can lead to more human intervention in the forest ecosystem [126]. To prepare the distance from roads map, Open Street Map (OSM) maps at a scale of 1:100,000 were used. The map of the distribution of villages in Iran at a scale of 1:100,000 was used to prepare the distance from residential areas map. The Euclidean distance of residential areas and roads to forests was then calculated in 30 × 30 m pixel size using Arc GIS 10.6 software.

Land cover, whether forest, agricultural land, or impermeable surface, is used to measure the flammability of an area [51]. The land cover is usually known as fuel for the fire. The combination of Sentinel-1 and Sentinel-2 data products in GEE was used for land cover analysis. The land cover data were prepared in the GEE platform [43,127,128].

Vegetation is considered fuel for wildfires, and NDVI is an index used in most studies to evaluate this factor [92–94]. The NDVI was calculated using the OLI Landsat-8 images in the GEE platform using Equation (4). The annual average of Landsat-8 images in 2021 was used to prepare NDVI.

$$NDVI = (NIR - RED)/(NIR + RED) \quad (4)$$

NIR and RED denote the near-infrared and visible red bands, respectively. The NIR band (0.85–0.88 μm) and RED band (0.64–0.67 μm) were used from Landsat-8 images.

2.4. Wildfire Susceptibility Methods

Before modeling, the values of effective criteria were normalized between 0 and 1, and then 70% were considered as training data and 30% were considered as validation data. Specifically, a Windows 10 desktop PC with an Intel i7 processor, 16 GB of RAM, and the required software were used to execute the calculations. The deep learning algorithms were developed using the Python programming language in the Google Colab (https://colab.research.google.com/) (launched by Google in 12 October 2017) platform.

2.4.1. Recurrent Neural Network (RNN)

Equipped with parameter sharing and graph-unrolling schemes, an RNN is a typical class of deep learning models that create a sequence and serve as the structural block of other productive deep learning architectures, enabling the plotting of relationships and dependencies between molecular character sequences of arbitrary lengths by incorporating the concept of time or order into the model [129]. Recurrent Neural Networks (RNNs) are deep learning algorithms that have received significant attention due to their ability to effectively process sequential data [66,130,131]. RNNs consist of layers, learnable parameters, and error functions [68]. RNN employs a recursive approach to effectively capture the temporal correlations and dynamic nature of the data. During the training process, the network parameters are determined by utilizing sampled data [132]. The layers of an RNN include an input layer, one or multiple hidden layers, and an output layer [133,134]. Initially, the input layer receives input data related to wildfire conditions. Then, these data are processed and analyzed in the hidden layers. The hidden layers, using weights and activation functions, perform sequential transformations to generate more complex features and produce discriminative features with enhanced distinguishability [135]. In a recurrent neural network, the network retains information from previous inputs and incorporates it in the computation of the current output. Unlike in convolutional neural networks where nodes between hidden layers are disconnected, in recurrent neural networks, these nodes are connected, and the input to the hidden layers includes both the output of the input layer and the output of the hidden layer from the previous moment [133,134,136].

The role of the output layer is to receive results based on the features obtained in the last hidden layer. It is also responsible for interpreting important and discriminative features to provide final results, which is achieved through an activation function [137]. Ultimately, each unit in the hidden layer is connected to other units, and information is transmitted from one layer to the next in the network [138].

The basic RNN's hidden units can be represented by Equations (5) and (6).

$$h_t = f(W_x x_t + W_h h_{t-1} + b_h) \quad (5)$$

$$y = W_y + by \quad (6)$$

where xt is the input data and ht denotes the hidden state in time t (seconds). This value is summed up with the stage's bias by the cell state in the previous stage, which is shown with h(t − 1) in time t − 1 and input data x(t − 1).

In the equation above, Wx and Wh of the coefficients and activator function can be tanh or ReLU. RNN uses constant weights for calculations in all repeated modes. The output of RNN is related to the input data in the current time and calculations in the hidden state of the previous time. The RNN architecture can be changed depending on different needs. An RNN can be converted to a deep RNN by increasing the chain length of hidden layers and adding the depth between the input to hidden, hidden to hidden, and hidden to output layers [139]. According to the findings, a deep RNN acts better than a shallow one since it can remarkably reduce the long-term dependencies of the input dataset. In other words, as the model's depth increases, the relationships between hidden states over time strengthen, enabling the model to better learn complex patterns and long-term dependencies [139].

In this study, an RNN model was implemented using the Keras library with a simple RNN layer architecture. The model consists of a simple RNN layer, a dropout layer to prevent overfitting, and two fully connected layers with the ReLU activation function. The 'Adam' optimization algorithm was used to train the RNN algorithm [140].

2.4.2. Long Short-Term Memory (LSTM)

LSTM has been designed to prevent the problem of long-term dependence and memorize information for long periods [141]. LSTM is the development of RNN. To overcome the training problems of RNNs, LSTMs can learn long-term dependencies and prevent exploding and vanishing gradients [142]. LSTM (Long Short-Term Memory) has a similar overall structure to RNN, consisting of an input layer, one or multiple hidden layers, and an output layer [143]. However, in LSTM, the basic RNN unit is replaced with a memory block, which is referred to as an LSTM cell [144].

The memory block of an LSTM has an input gate, a forget gate, and an output gate, which adjust the flow of information inside and outside a cell [145]. By utilizing these three gating mechanisms, LSTM is capable of controlling the flow of information and memory over time, enabling it to understand long-term dependencies in sequential data [143].

The input gate is the controller of input information to the cell state. The importance of the output information of the forget gate is updated using Equation (7). The output gate is responsible for combining the derived information using Equation (10). In Equation (9), g_t in the LSTM architecture is related to the previous cell's hidden (h) and C modes, which act as the memory.

$$f_t = \sigma(W_f X_t + R_f H_{t-1} + b_f) \quad (7)$$

$$i_t = \sigma(W_i X_t + R_i H_{t-1} + b_i) \quad (8)$$

$$g_t = \tanh(W_g X_t + R_g H_{t-1} + b_g) \quad (9)$$

$$o_t = \sigma(W_0 X_t + R_o H_{t-1} + b_o) \quad (10)$$

The sigmoid function, represented as σ in the above formulas. The input gate in LSTM serves as a controller for inputting information into the cell state. In LSTM, each LSTM unit comprises a hidden state and a cell state. The Hidden State is referred to as the short-term memory, while the Cell State represents the long-term memory. The Hidden State, denoted by H_t, is associated with the previous time step (t − 1), and the current time step (t). The Cell State, denoted by ct, represents the current time step, while ct − 1 represents the Cell State from the previous time step. Deep learning algorithms perform analysis on the Cell State, determining the importance of retaining or forgetting information. This stage is crucial as the model decides whether to forget or store the data. In this structure, in time

step t, the cell is fed with input H_t and hidden mode H (t − 1). Output mode Ct and hidden mode H_t are given in time step t.

$$C_t = f_t * C_{t-1} + i_t * g_t \tag{11}$$

$$H_t = o_t * \sigma_c(C_t) \tag{12}$$

This study utilizes the LSTM layer implemented using the Keras library to extract important features from the data. Dropout and Dense layers were employed to enhance the flexibility and generalization power of the model. The Adam optimization algorithm is chosen for training and improving the model's performance [146].

2.4.3. Multicollinearity Analysis

After selecting the influential factors and incorporating them into deep learning algorithms, it is important to examine the presence of multicollinearity among these factors. Multicollinearity refers to the correlation between two or more independent factors, which can lead to errors in the results [147,148]. One way to assess multicollinearity in the modeling process is by using the variance inflation factor (VIF) method [149,150]. VIF values greater than ten suggest the presence of multicollinearity among the criteria, and such criteria should not be included in the modeling [151].

2.4.4. Feature Importance Using Gini Index

The random forest (RF) algorithm was introduced by Ho (1994) and was later developed by Breiman et al. (2001) [152,153]. RF is a combination of several decision trees that can produce multiple predictions using independent algorithms. In line with previous studies, the average Gini index was used to achieve the best classification of input data and to determine the weight of influential factors [154–157]. This index enables the evaluation of factors that are influential in wildfires, and the identification of prediction patterns in large volumes of data [158,159]. It should be noted that this approach can help overcome the limitations of traditional statistical methods and improve the accuracy of wildfire prediction models. The Gini index numerically expresses the division quality of a particular node (class) on a variable (feature) such that the division would be the best one along that feature. This index also determines the dependence between features. The Gini index's lowest value indicates each node's best division [160]. If dataset D includes instances of class D, the Gini index can be obtained from Equation (13) [161].

$$\text{gini}(D) = 1 - \sum_{c=1}^{C} P_c^2 \tag{13}$$

In this equation, Pc is the relative frequency of class C in dataset (node) D, indicating the distribution of class labels in a node. The number of trees used in the RF model, which was set to 100 after considering computational efficiency and model performance; the proportion of data used to generate each tree, which was 70% of the original training dataset sampled through bootstrap aggregating; the parameter settings were employed to limit over fittings, such as a maximum tree depth of ten and a minimum of five samples per leaf node.

2.4.5. Validation

The MSE was used to evaluate the modeling accuracy by LSTM and RNN models, and the ROC and area under the curve (AUC) were used to examine the wildfire susceptibility maps. Overall, 30% of the wildfire data not used in the modeling were used to evaluate the wildfire susceptibility maps. Of the wildfire data, 30%, which were not used in the modeling, were employed to evaluate the wildfire sensitivity maps.

- MSE

The MSE index is used as an error evaluation criterion between observed and predicted instances (Equation (14)) [159].

$$\mathrm{MSE} = \frac{\sum_{i=1}^{n}(y_i - \hat{y}_i)^2}{n} \quad (14)$$

- ROC and AUC

When binary (zero and one) classification is used for forest and non-wildfire areas in modeling methods (LSTM and RNN), validation requires a confusion matrix for each model. This index obtains the number of points correctly or incorrectly identified as forest or non-wildfire areas [51]. The ROC curve graphically indicates the sensitivity and specificity of the threshold values of the classification obtained from models [126]. The *X*-axis indicates the false positive rate (specificity-1), while the *Y*-axis indicates the real positive rate (sensitivity) in the ROC curve [149,162,163] (Equations (15) and (16)).

$$X = 1 - \left(\frac{\text{True Negative(TN)}}{\text{True Negative(TN)} + \text{False Poditive(FN)}}\right) \quad (15)$$

$$Y = \left(\frac{\text{True Psotive(TP)}}{\text{True Positive(TP)} + \text{False Negative(FN)}}\right) \quad (16)$$

In Equations (15) and (16), TP indicates the number of wildfires classified as wildfires, TN denotes the number of wildfires classified as non-wildfires, FP is the number of non-wildfire areas incorrectly classified as wildfire ones, and FN is the number of wildfire areas incorrectly classified as non-wildfire [128].

AUC varies from 0.5 to 1. Higher values of AUC indicate a better resolution of classification, while lower values indicate a worse resolution [164].

3. Results

3.1. Result of Multicollinearity

Based on the results of the VIF index (Table 1), the most multicollinearity was related to the criteria of wind speed (6.17), rainfall (5.74), temperature (4.43), altitude (2.49), slope (2.35), TWI (2.18), wind effect (1.74), distance to the road (1.67), distance to residential areas (1.35), land cover (1.35), NDVI (1.24), and aspect (1.03), respectively. The results showed that the value of the VIF index for all factors that affect wildfire is less than ten, and all factors can participate in the modeling of wildfire susceptibility.

Table 1. Result of multicollinearity in wildfire factors.

Factors	VIF
NDVI	1.24
Wind effect	1.74
TWI	2.18
Slope	2.35
Aspect	1.03
Wind speed	6.17
Land cover	1.35
Altitude	2.49
Distance to residential areas	1.35
Distance to road	1.67
Rainfall	5.74
Temperature	4.43
Factors	VIF

3.2. Determining the Importance of Factors Affecting Wildfires

The results of the importance of criteria using the Gini index in Landsat-8 and MODIS datasets are summarized in Table 2. The results showed that in the Landsat-8 dataset, the criteria of temperature (0.2), wind speed (0.15), and TWI (0.13) had the most significant impact, and the criteria of wind effect (0.062), distance to residential areas (0.056), and aspect (0.041) had the most negligible impact on the occurrence of wildfires. According to the findings, the criteria of temperature (0.12), TWI (0.098), and slope (0.076) had the most significant impact on the occurrence of wildfires in the MODIS dataset. In contrast, the criteria of aspect (0.019), rainfall (0.014), and distance to residential areas (0.009) had the lowest impact.

Table 2. Result of the importance of factors affecting wildfires.

Factors	Landsat-8 Dataset	MODIS Dataset
NDVI	0.073	0.05
Wind effect	0.062	0.021
TWI	0.13	0.098
Slope	0.11	0.076
Aspect	0.041	0.019
Wind speed	0.16	0.063
Land cover	0.09	0.035
Altitude	0.07	0.033
Distance to residential areas	0.056	0.009
Distance to road	0.063	0.025
Rainfall	0.08	0.014
Temperature	0.2	0.12

3.3. Wildfire Susceptibility Modeling with Deep Learning Algorithms

Modeling was conducted on two datasets (Landsat-8 and MODIS), and the results of modeling evaluation on the data of train and validation are summarized in Table 3. The MSE index was used to assess the accuracy of the algorithms.

Table 3. Result of modeling with deep learning algorithms.

Dataset	LSTM		RNN	
	Train	Validation	Train	Validation
Landsat-8	0.172	0.177	0.175	0.177
MODIS	0.204	0.227	0.201	0.219

The results showed that the value of the MSE index in the LSTM algorithm for the Landsat-8 dataset was 0.172 for train data and 0.177 for validation data. Additionally, in the MODIS dataset, the accuracy of the LSTM algorithm for training and validation data was equal to 0.204 and 0.227, respectively. The RNN algorithm findings showed that the training data values for Landsat-8 and MODIS were 0.175 and 0.201, respectively, while the validation data values were 0.177 and 0.219, respectively. Based on the modeling results with two deep learning algorithms, the accuracy of the Landsat-8 dataset was higher than MODIS. In the MODIS dataset, the modeling accuracy of the RNN algorithm was higher than LSTM in training and validation data. In contrast, in the Landsat-8 dataset, the values of these two algorithms were equal in validation data, and LSTM accuracy was better than RNN in training data.

3.4. Wildfire Susceptibility Mapping

After modeling with two deep learning algorithms on Landsat-8 and MODIS datasets, the results were applied to the entire study area, and four susceptibility maps were created. The four prepared susceptibility maps were divided into five risk classes from very low to

very high using the natural breaks classification method (Figure 6a–d). Based on susceptibility maps in the MODIS dataset, the study areas northwest, north, and east are prone to wildfires. The susceptibility maps in the Landsat-8 dataset showed that the wildfire-prone areas are similar to the MODIS dataset and differ in terms of the extent percentage.

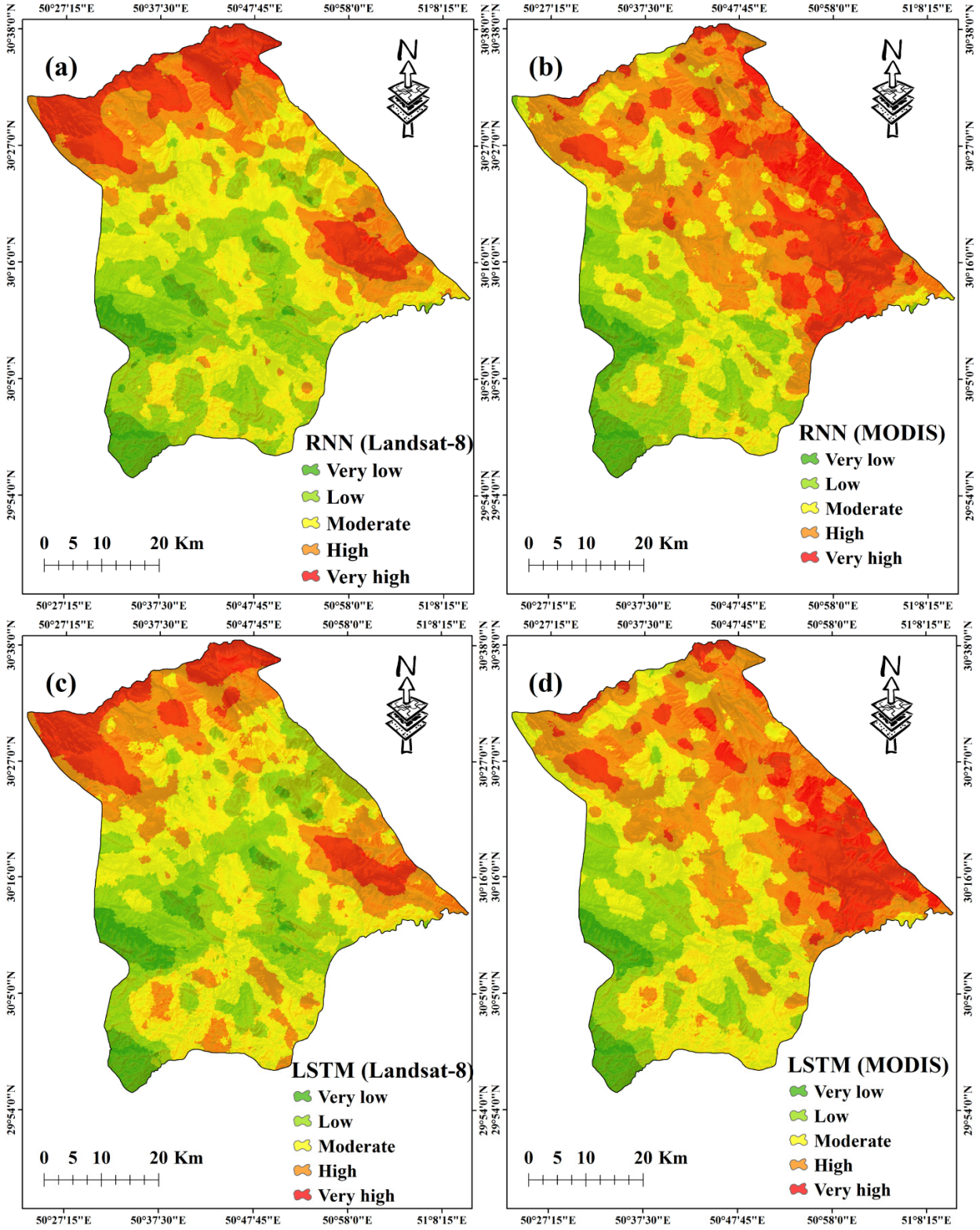

Figure 6. Wildfire susceptibility mapping by: (**a**) RNN (landsat-8); (**b**) RNN (MODIS); (**c**) LSTM (Landsat-8); and (**d**) LSTM (MODIS).

Figure 7 shows the percentage of wildfire susceptibility classes generated by each algorithm. The RNN (Landsat-8) classifies 14.6% of the very high susceptibility class area, 18.2% in high, 34% in moderate, 27.1% in low, and 6.1% in very low. Similarly to the RNN (MODIS), the very low, low, moderate, high, and very high classes correspond to 4.7, 15.5, 25, 33.4, and 21.4%, respectively. With the LSTM (MODIS), these percentages are similar: 4.1%, 13.5%, 32.22%, 33.9%, and 16.28%. Additionally, the LSTM (Landsat-8) algorithm showed that the moderate (34.9%), low (26.05%), high (21.22%), very high (11.33%), and very low (6.5%) classes have the highest risk percentage, respectively. The results showed that RNN (MODIS), LSTM (MODIS), RNN (Landsat-8), and LSTM (Landsat-8) algorithms had the highest percentage in the very high-risk category, respectively.

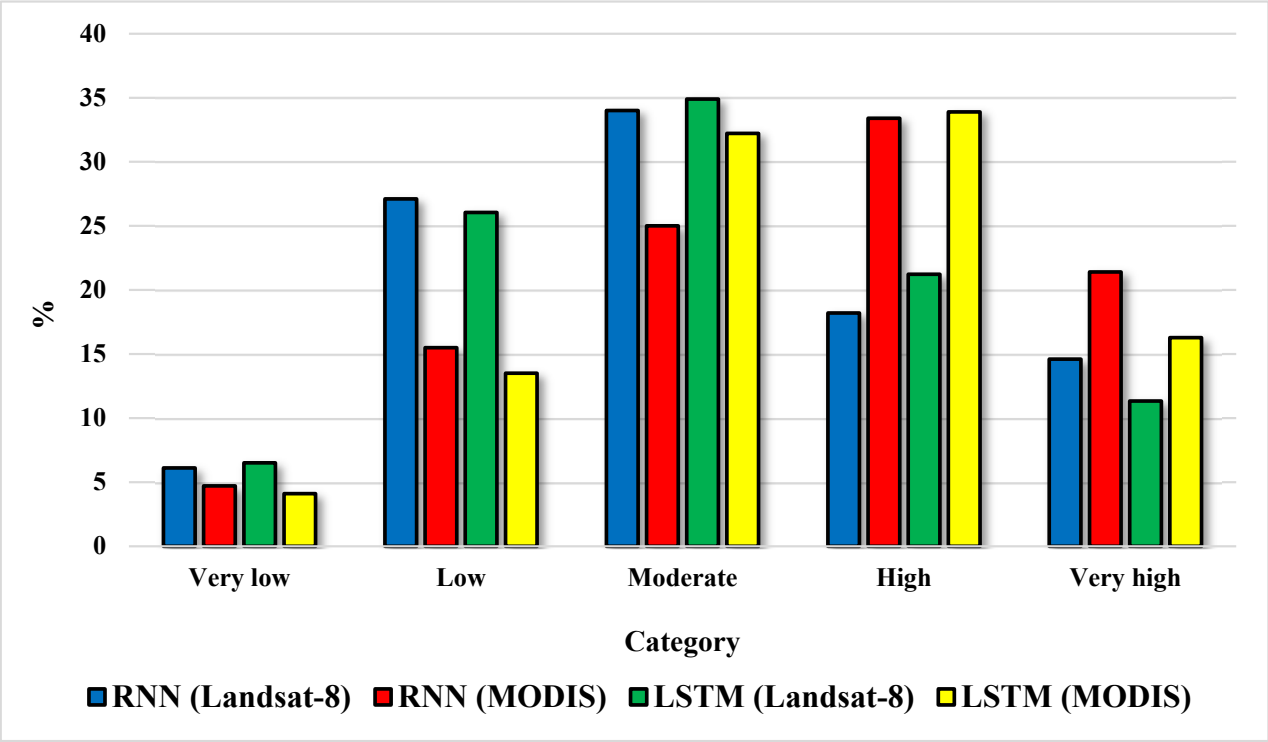

Figure 7. Percentage of risky areas in wildfire susceptibility maps.

3.5. Validation of Models and Susceptibility Maps

The susceptibility maps of two deep learning algorithms were evaluated in two datasets using 30% of the data and the ROC curve. The results of this evaluation are shown in Table 4 and Figure 8. The results of the AUC index showed that the highest accuracy was related to RNN (MODIS) (97.1%), RNN (Landsat-8) (96.6%), LSTM (MODIS) (96.4%), and LSTM (Landsat-8) (94.1%) algorithms, respectively.

Table 4. Result of AUC index in in four wildfire susceptibility models.

Algorithms	AUC	Standard Error	95% CI
LSTM (Landsat-8)	0.941	0.00640	0.926 to 0.954
RNN (Landsat-8)	0.966	0.00463	0.954 to 0.976
LSTM (MODIS)	0.964	0.00874	0.939 to 0.981
RNN (MODIS)	0.971	0.00776	0.948 to 0.985

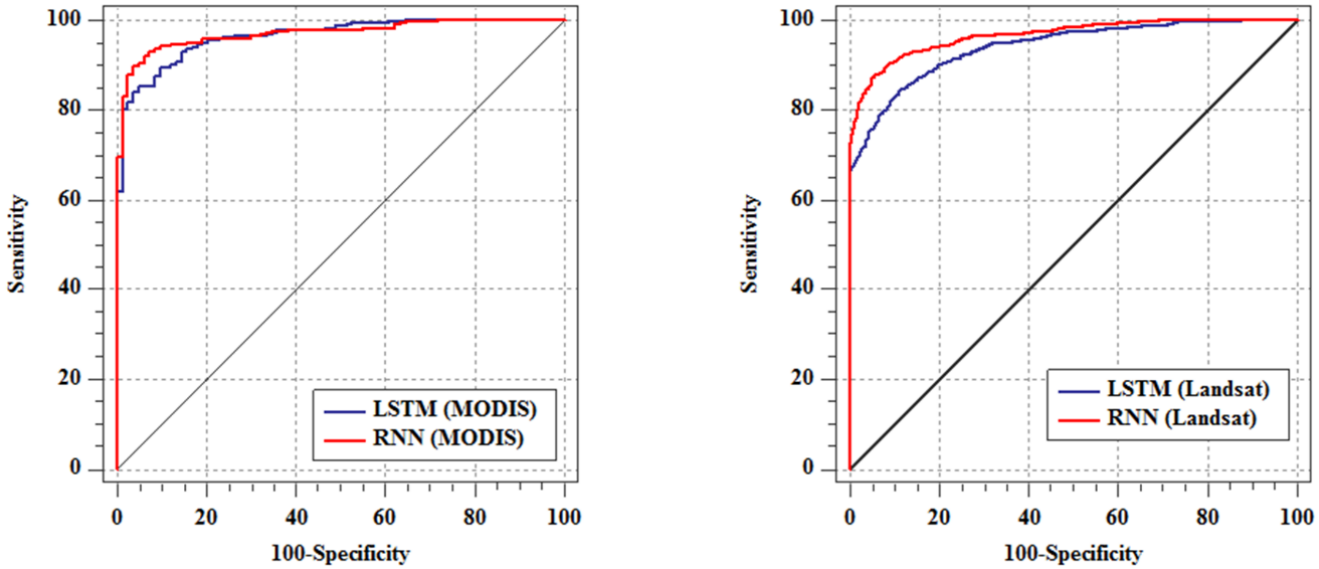

Figure 8. ROC curve results in four wildfire susceptibility models.

4. Discussion

Based on the results, two deep learning algorithms were highly accurate in modeling (AUC > 0.9). Deep learning provides numerous benefits, including higher accuracy, more effective feature engineering, adaptability, scalability, and improved natural language processing and computer vision [165]. The results showed that the RNN algorithm was more accurate than the LSTM algorithm in two datasets for preparing the wildfire susceptibility map. RNNs have an advantage over LSTMs in that they are more straightforward and less computationally expensive, making them faster to train and easier to interpret [166]. The flexibility, memory, parallelization, and interpretability of RNNs make them suited for a wide range of sequence modeling and prediction problems [167]. Among the two datasets, deep learning algorithms in the MODIS dataset had higher accuracy than the Landsat-8 dataset. The advantages of MODIS compared to Landsat-8 include broader coverage, higher temporal resolution, coarser spatial resolution in large-scale phenomena, and improved atmospheric correction [168]. Overall, remote sensing can significantly improve the speed and accuracy of wildfire detection and monitoring, helping to reduce the damage caused by wildfires and protect human lives and wildlife [169].

The comparison of the accuracies obtained in this research with other researchers is summarized in Table 5. According to the obtained results, the accuracy of the RNN algorithm for both the MODIS and Landsat-8 images is 97.1% and 96.6%, respectively. The LSTM model achieves accuracies of 96.4% and 94.1% for the aforementioned images, respectively. Referring to the Table 4 and previous research in the field of deep learning for wildfire susceptibility mapping, The RNN algorithm employed in this study demonstrates slightly lower accuracy compared to both the DCN_Fire model, achieving 98.3% accuracy, and the GRU model, which achieves an even higher accuracy of 99.89%. The employed LSTM algorithm in this study exhibits a comparable accuracy to the Multi-AM-LSTM model, both achieving an accuracy of approximately 96%. Among the mentioned models, the CNN model achieves an accuracy of 87.92%, the DNN model achieves 75.14%, and the LSTNet model achieves 94.1%, and all three of these models have lower accuracy compared to both LSTM and Multi-AM-LSTM models in our study.

Table 5. Comparison of modeling accuracies of this research with past research.

Model Name	Reference	Study Area	Best Model (Accuracy %)	Accuracy of Our Study Models (Accuracy %)
DCN_Fire, Kim's CNN model, AlexNet, Eight-layer CNN + Fisher vector, HOG + SVM, Deep belief net + neural net	[170]	Guangdong Province, China	DCN_Fire (98.3)	RNN (MODIS) = 97.1 LSTM (MODIS) = 96.4
RNN, LSTM, GRU	[141]	data	GRU (99.89)	RNN (MODIS) = 97.1 LSTM (MODIS) = 96.4
LSTM, LSTNet, RNN, SVR	[171]	Chongli, China	LSTNet (94.1)	RNN (MODIS) = 97.1 LSTM (MODIS) = 96.4
VM, XGBoost, NN, RNN, LSTM, Multi-AM-LSTM	[172]	Montesinho Natural Park, Portuguese	Multi-AM-LSTM (96)	RNN (MODIS) = 97.1 LSTM (MODIS) = 96.4
Logistic Regression, DNN, KFRI (Fire Risk Index)	[173]	South Korea	DNN (75.14)	RNN (MODIS) = 97.1 LSTM (MODIS) = 96.4
ANN, SVM, RF	[174]	Amol County, Iran	RF (88)	RNN (MODIS) = 97.1 LSTM (MODIS) = 96.4
CNN, SiameseNet, Multi-head CNN, VAE, XGBoost, SVM, Ensemble	[53]	Biobío and Ñuble regions, Chile	Ensemble (95.3)	RNN (MODIS) = 97.1 LSTM (MODIS) = 96.4
FDA, GLM, SVM	[175]	Chaharmahal and Bakhtiari Province, Iran	GLM (83.7)	RNN (MODIS) = 97.1 LSTM (MODIS) = 96.4
EO-GBDT, ANN, RF, DT, SVM, NB, LR, GBDT, PSO-SVM	[52]	Nanda Devi, India	EO-GBDT (95)	RNN (MODIS) = 97.1 LSTM (MODIS) = 96.4
ANFIS-GA-SA, RBF-ICA	[176]	Chaharmahal and Bakhtiari Province, Iran	ANFIS-GA-SA (90.3)	RNN (MODIS) = 97.1 LSTM (MODIS) = 96.4
GAM, MARS, SVM, GAM-MARS-SVM	[177]	Golestan Province, Iran	GAM-MARS-SVM (83)	RNN (MODIS) = 97.1 LSTM (MODIS) = 96.4
FR-MLP, FR-LR, FR-CART, FR-SVM, FR-RF	[178]	Tanger-T'etouan-Al Hoceima region, North of Morocco	RF-FR (90.4)	RNN (MODIS) = 97.1 LSTM (MODIS) = 96.4
CNN, RF, SVM, MLP, KLR	[76]	Yunnan Province of China	CNN (87.92)	RNN (MODIS) = 97.1 LSTM (MODIS) = 96.4

Regarding the development of wildfire risk prediction models in the field of machine learning, the RF-FR model achieves an accuracy of 90.4%, GAM-MARS-SVM model achieves 83.0% accuracy, ANFIS-GA-SA model achieves 90.3% accuracy, GLM model achieves 83.7% accuracy, and RF model achieves 88.0% accuracy. However, all of these models have lower accuracy compared to both mentioned algorithms in our study. Among the machine learning models, EO-GBDT and the proposed Ensemble model by Bjånes et al. achieve higher accuracies of 95% and 95.3%, respectively, compared to the LSTM algorithm in our study, which demonstrates their superior performance on the Landsat-8 images.

In general, and based on two datasets, the parameters of temperature, wind speed, slope, and TWI had a more significant impact on the occurrence of wildfires in the study area. The occurrence and behavior of wildfires are greatly influenced by temperature. An increase in wildfires' likelihood, intensity, difficulty to contain, and their effect on air quality and human health has been linked to rising global temperatures [179]. Higher winds can

increase the likelihood of flames, make them harder to extinguish and alter a fire's behavior, intensity, and spread [180]. Wildfires tend to be less severe in places with higher TWI values, while ignition, fire spread, and fire severity tend to be higher in areas with lower TWI values [143]. Wildfires are more likely to spread and be destructive on steep slopes because more material is needed to burn [181].

Limitations and Future Recommendations

The preparation of wildfire risk and hazard maps is inherently subject to uncertainties, stemming from various stages of modeling and environmental conditions. Uncertainty arises in terms of input data, monitoring of wildfires through satellite imagery, as well as prediction and analysis carried out by algorithms.

Noise in the data, data scaling irregularities, insufficient samples, or measurement errors are factors contributing to uncertainty in the input data of fire-affected areas caused by wildfires [182].

Choosing the wrong algorithm, improper parameter configuration, limited availability of training data, selecting inappropriate features, and inadequate model generalization are all factors that contribute to the presence of uncertainty in the algorithm's prediction and analysis [182].

Our recommendation for future research is to consider this uncertainty in various modeling approaches for forest wildfire. Despite the extensive research conducted on modeling and predicting wildfires, there is still no absolute certainty in these models due to their complexity and the multitude of factors influencing fire occurrences. Therefore, in order to enhance the accuracy and predictive capabilities of these models, it is essential to pay attention to this uncertainty in future research and employ improved and advanced methods for modeling wildfires.

5. Conclusions

This research examined two remote sensing datasets (Landsat-8 and MODIS) for wildfire monitoring and used these two datasets to model wildfire susceptibility with two deep learning algorithms (RNN and LSTM). The results showed that the parameters of temperature, wind speed, and slope are more critical in the occurrence of wildfires. Among the deep learning algorithms, the RNN algorithm had higher accuracy than the LSTM algorithm in both datasets. Additionally, the MODIS dataset had higher accuracy than the Landsat-8 dataset in modeling wildfire susceptibility. The results showed that the northern and eastern regions of the study area are more prone to wildfires. Wildfire risk maps can help local managers and planners better control and manage wildfires. Despite the advantages of this research in data and modeling, it had limitations, such as not using the feature selection method and not optimally determining the parameters of deep learning algorithms. Therefore, suggestions for future research include using other deep learning algorithms, using a feature selection method in modeling, determining the optimal parameters of deep learning algorithms with metaheuristic algorithms, and using different remote sensing images for wildfire monitoring and data fusion in the modeling provided.

Author Contributions: Conceptualization, N.B. and S.V.R.-T.; Data curation, N.B.; Formal analysis, N.B., S.V.R.-T. and K.M.A.-K.; Funding acquisition, A.S.-N. and S.-M.C.; Investigation, S.V.R.-T.; Methodology, N.B. and T.A.; Project administration, A.S.-N. and S.-M.C.; Resources, K.M.A.-K. and B.N.; Software, N.B. and S.V.R.-T.; Supervision, A.S.-N.; Validation, T.A. and N.B.; Visualization, S.V.R.-T.; Writing—original draft, N.B.; Writing—review & editing, S.V.R.-T., K.M.A.-K., A.S.-N., T.A., B.N. and S.-M.C. All authors have read and agreed to the published version of the manuscript.

Funding: This research was supported by the MSIT (Ministry of Science and ICT), Korea, under the ITRC (Information Technology Research Center) support program (IITP-2023-RS-2022-00156354) supervised by the IITP (Institute for Information & communications Technology Planning & Evaluation) and the Ministry of Trade, Industry and Energy (MOTIE) and Korea Institute for Advancement of Technology (KIAT) through the International Cooperative R&D program (Project No. P0016038).

Institutional Review Board Statement: Not applicable.

Informed Consent Statement: Not applicable.

Data Availability Statement: The data that support the findings of this study are available from the corresponding author, [A.S.-N.], upon reasonable request.

Conflicts of Interest: The authors declare no conflict of interest.

References

1. Oom, D.; Pereira, J.M. Exploratory spatial data analysis of global MODIS active fire data. *Int. J. Appl. Earth Obs. Geoinf.* **2013**, *21*, 326–340. [CrossRef]
2. Hantson, S.; Pueyo, S.; Chuvieco, E. Global fire size distribution: From power law to log-normal. *Int. J. Wildland Fire* **2016**, *25*, 403–412. [CrossRef]
3. Li, J.; Shan, Y.; Yin, S.; Wang, M.; Sun, L.; Wang, D. Nonparametric multivariate analysis of variance for affecting factors on the extent of wildfire damage in Jilin Province, China. *J. For. Res.* **2019**, *30*, 2185–2197. [CrossRef]
4. Zema, D.A.; Nunes, J.P.; Lucas-Borja, M.E. Improvement of seasonal runoff and soil loss predictions by the MMF (Morgan-Morgan-Finney) model after wildfire and soil treatment in Mediterranean forest ecosystems. *Catena* **2020**, *188*, 104415. [CrossRef]
5. Santana, V.M.; Alday, J.G.; Baeza, M.J. Mulch application as post-fire rehabilitation treatment does not affect vegetation recovery in ecosystems dominated by obligate seeders. *Ecol. Eng.* **2014**, *71*, 80–86. [CrossRef]
6. Adab, H.; Kanniah, K.D.; Solaimani, K. Modeling wildfire risk in the northeast of Iran using remote sensing and GIS techniques. *Nat. Hazards* **2013**, *65*, 1723–1743. [CrossRef]
7. Shiravand, H.; Hosseini, S.A. A new evaluation of the influence of climate change on Zagros oak forest dieback in Iran. *Theor. Appl. Climatol.* **2020**, *141*, 685–697. [CrossRef]
8. Feizizadeh, B.; Omarzadeh, D.; Mohammadnejad, V.; Khallaghi, H.; Sharifi, A.; Karkarg, B.G. An integrated approach of artificial intelligence and geoinformation techniques applied to wildfire risk modeling in Gachsaran, Iran. *J. Environ. Plan. Manag.* **2023**, *66*, 1369–1391. [CrossRef]
9. Jaafari, A.; Termeh, S.V.R.; Bui, D.T. Genetic and firefly metaheuristic algorithms for an optimized neuro-fuzzy prediction modeling of wildfire probability. *J. Environ. Manag.* **2019**, *243*, 358–369. [CrossRef] [PubMed]
10. Adab, H. Landfire hazard assessment in the Caspian Hyrcanian forest ecoregion with the long-term MODIS active fire data. *Nat. Hazards* **2017**, *87*, 1807–1825. [CrossRef]
11. Xu, R.; Lin, H.; Lu, K.; Cao, L.; Liu, Y. A wildfire detection system based on ensemble learning. *Forests* **2021**, *12*, 217. [CrossRef]
12. Zhang, J.; Li, W.; Yin, Z.; Liu, S.; Guo, X. Wildfire detection system based on wireless sensor network. In Proceedings of the 2009 4th IEEE Conference on Industrial Electronics and Applications, Xi'an, China, 25–27 May 2009; pp. 520–523.
13. Yu, L.; Wang, N.; Meng, X. Real-time wildfire detection with wireless sensor networks. In Proceedings of the 2005 International Conference on Wireless Communications, Networking and Mobile Computing, Wuhan, China, 26 September 2005; pp. 1214–1217.
14. Chen, S.-J.; Hovde, D.C.; Peterson, K.A.; Marshall, A.W. Fire detection using smoke and gas sensors. *Fire Saf. J.* **2007**, *42*, 507–515. [CrossRef]
15. Lee, B.; Kwon, O.; Jung, C.; Park, S. The development of UV/IR combination flame detector. *J. KIIS* **2001**, *16*, 140–145.
16. Kang, D.; Kim, E.; Moon, P.; Sin, W.; Kang, M.-g. Design and analysis of flame signal detection with the combination of UV/IR sensors. *J. Internet Comput. Serv.* **2013**, *14*, 45–51. [CrossRef]
17. Hendel, I.-G.; Ross, G.M. Efficacy of remote sensing in early wildfire detection: A thermal sensor comparison. *Can. J. Remote Sens.* **2020**, *46*, 414–428. [CrossRef]
18. Varotsos, C.A.; Krapivin, V.F.; Mkrtchyan, F.A. A new passive microwave tool for operational wildfires detection: A case study of siberia in 2019. *Remote Sens.* **2020**, *12*, 835. [CrossRef]
19. Pradhan, B.; Al-Najjar, H.A.; Sameen, M.I.; Tsang, I.; Alamri, A.M. Unseen land cover classification from high-resolution orthophotos using integration of zero-shot learning and convolutional neural networks. *Remote Sens.* **2020**, *12*, 1676. [CrossRef]
20. Gibril, M.B.A.; Kalantar, B.; Al-Ruzouq, R.; Ueda, N.; Saeidi, V.; Shanableh, A.; Mansor, S.; Shafri, H.Z. Mapping heterogeneous urban landscapes from the fusion of digital surface model and unmanned aerial vehicle-based images using adaptive multiscale image segmentation and classification. *Remote Sens.* **2020**, *12*, 1081. [CrossRef]
21. You, W.; Lin, L.; Wu, L.; Ji, Z.; Zhu, J.; Fan, Y.; He, D. Geographical information system-based wildfire risk assessment integrating national forest inventory data and analysis of its spatiotemporal variability. *Ecol. Indic.* **2017**, *77*, 176–184. [CrossRef]
22. Fernandes, A.M.; Utkin, A.B.; Lavrov, A.V.; Vilar, R.M. Development of neural network committee machines for automatic wildfire detection using lidar. *Pattern Recognit.* **2004**, *37*, 2039–2047. [CrossRef]
23. Jaiswal, R.K.; Mukherjee, S.; Raju, K.D.; Saxena, R. Wildfire risk zone mapping from satellite imagery and GIS. *Int. J. Appl. Earth Obs. Geoinf.* **2002**, *4*, 1–10.
24. Erten, E.; Kurgun, V.; Musaoglu, N. Wildfire risk zone mapping from satellite imagery and GIS: A case study. In Proceedings of the XXth Congress of the International Society for Photogrammetry and Remote Sensing, Istanbul, Turkey, 15 July 2004; pp. 222–230.

25. Pradhan, B.; Awang, M.A. Application of remote sensing and gis for wildfire susceptibility mapping using likelihood ratio model. *Proc. Map Malays.* **2007**, *16*, 3.
26. Schroeder, W.; Oliva, P.; Giglio, L.; Quayle, B.; Lorenz, E.; Morelli, F. Active fire detection using Landsat-8/OLI data. *Remote Sens. Environ.* **2016**, *185*, 210–220. [CrossRef]
27. Zhang, T.; Wooster, M.J.; Xu, W. Approaches for synergistically exploiting VIIRS I-and M-Band data in regional active fire detection and FRP assessment: A demonstration with respect to agricultural residue burning in Eastern China. *Remote Sens. Environ.* **2017**, *198*, 407–424. [CrossRef]
28. Gargiulo, M. Advances on CNN-based super-resolution of Sentinel-2 images. In Proceedings of the IGARSS 2019–2019 IEEE International Geoscience and Remote Sensing Symposium, Yokohama, Japan, 28 July–2 August 2019; pp. 3165–3168.
29. Konkathi, P.; Shetty, A. Inter comparison of post-fire burn severity indices of Landsat-8 and Sentinel-2 imagery using Google Earth Engine. *Earth Sci. Inform.* **2021**, *14*, 645–653. [CrossRef]
30. Lyon, J.G.; Yuan, D.; Lunetta, R.S.; Elvidge, C.D. A change detection experiment using vegetation indices. *Photogramm. Eng. Remote Sens.* **1998**, *64*, 143–150.
31. Shang, X.; Song, M.; Wang, Y.; Yu, C.; Yu, H.; Li, F.; Chang, C.-I. Target-constrained interference-minimized band selection for hyperspectral target detection. *IEEE Trans. Geosci. Remote Sens.* **2020**, *59*, 6044–6064. [CrossRef]
32. Wang, P.; Wang, L.; Leung, H.; Zhang, G. Super-resolution mapping based on spatial–spectral correlation for spectral imagery. *IEEE Trans. Geosci. Remote Sens.* **2020**, *59*, 2256–2268. [CrossRef]
33. Pradhan, B.; Suliman, M.D.H.B.; Awang, M.A.B. Wildfire susceptibility and risk mapping using remote sensing and geographical information systems (GIS). *Disaster Prev. Manag. Int. J.* **2007**, *16*, 344–352. [CrossRef]
34. Lin, W.; Zhang, Z.; Zhang, L. Infrared moving small target detection and tracking algorithm based on feature point matching. *Eur. Phys. J. D* **2022**, *76*, 185. [CrossRef]
35. Hwang, C.-L.; Yoon, K. *Multiple Attribute Decision Making: Methods and Applications: A State-of-the-Art Survey*; Springer: Berlin/Heidelberg, Germany, 1981.
36. Chatterjee, P.; Chakraborty, S. A comparative analysis of VIKOR method and its variants. *Decis. Sci. Lett.* **2016**, *5*, 469–486. [CrossRef]
37. Goleiji, E.; Hosseini, S.M.; Khorasani, N.; Monavari, S.M. Wildfire risk assessment-an integrated approach based on multicriteria evaluation. *Environ. Monit. Assess.* **2017**, *189*, 612. [CrossRef]
38. Ljubomir, G.; Pamučar, D.; Drobnjak, S.; Pourghasemi, H.R. Modeling the spatial variability of wildfire susceptibility using geographical information systems and the analytical hierarchy process. In *Spatial Modeling in GIS and R for Earth and Environmental Sciences*; Elsevier: Amsterdam, The Netherlands, 2019; pp. 337–369.
39. Samui, P. Support vector machine applied to settlement of shallow foundations on cohesionless soils. *Comput. Geotech.* **2008**, *35*, 419–427. [CrossRef]
40. Jaafari, A.; Gholami, D.M.; Zenner, E.K. A Bayesian modeling of wildfire probability in the Zagros Mountains, Iran. *Ecol. Inform.* **2017**, *39*, 32–44. [CrossRef]
41. Hong, H.; Naghibi, S.A.; Moradi Dashtpagerdi, M.; Pourghasemi, H.R.; Chen, W. A comparative assessment between linear and quadratic discriminant analyses (LDA-QDA) with frequency ratio and weights-of-evidence models for wildfire susceptibility mapping in China. *Arab. J. Geosci.* **2017**, *10*, 167. [CrossRef]
42. Abedi Gheshlaghi, H.; Feizizadeh, B.; Blaschke, T. GIS-based wildfire risk mapping using the analytical network process and fuzzy logic. *J. Environ. Plan. Manag.* **2020**, *63*, 481–499. [CrossRef]
43. Nami, M.; Jaafari, A.; Fallah, M.; Nabiuni, S. Spatial prediction of wildfire probability in the Hyrcanian ecoregion using evidential belief function model and GIS. *Int. J. Environ. Sci. Technol.* **2018**, *15*, 373–384. [CrossRef]
44. Ganteaume, A.; Camia, A.; Jappiot, M.; San-Miguel-Ayanz, J.; Long-Fournel, M.; Lampin, C. A review of the main driving factors of wildfire ignition over Europe. *Environ. Manag.* **2013**, *51*, 651–662. [CrossRef]
45. Brownlee, J. Parametric and nonparametric machine learning algorithms. *Retrieved March* **2016**, *14*, 277–288.
46. Auret, L.; Aldrich, C. Interpretation of nonlinear relationships between process variables by use of random forests. *Miner. Eng.* **2012**, *35*, 27–42. [CrossRef]
47. Oliveira, S.; Oehler, F.; San-Miguel-Ayanz, J.; Camia, A.; Pereira, J.M. Modeling spatial patterns of fire occurrence in Mediterranean Europe using Multiple Regression and Random Forest. *For. Ecol. Manag.* **2012**, *275*, 117–129. [CrossRef]
48. Pourghasemi, H.R. GIS-based wildfire susceptibility mapping in Iran: A comparison between evidential belief function and binary logistic regression models. *Scand. J. For. Res.* **2016**, *31*, 80–98. [CrossRef]
49. Wittenberg, L.; Malkinson, D. Spatio-temporal perspectives of wildfires regimes in a maturing Mediterranean mixed pine landscape. *Eur. J. For. Res.* **2009**, *128*, 297–304. [CrossRef]
50. Tuyen, T.T.; Jaafari, A.; Yen, H.P.H.; Nguyen-Thoi, T.; Van Phong, T.; Nguyen, H.D.; Van Le, H.; Phuong, T.T.M.; Nguyen, S.H.; Prakash, I. Mapping wildfire susceptibility using spatially explicit ensemble models based on the locally weighted learning algorithm. *Ecol. Inform.* **2021**, *63*, 101292. [CrossRef]
51. Pham, B.T.; Jaafari, A.; Avand, M.; Al-Ansari, N.; Dinh Du, T.; Yen, H.P.H.; Phong, T.V.; Nguyen, D.H.; Le, H.V.; Mafi-Gholami, D. Performance evaluation of machine learning methods for wildfire modeling and prediction. *Symmetry* **2020**, *12*, 1022. [CrossRef]
52. Sachdeva, S.; Bhatia, T.; Verma, A. GIS-based evolutionary optimized Gradient Boosted Decision Trees for wildfire susceptibility mapping. *Nat. Hazards* **2018**, *92*, 1399–1418. [CrossRef]

53. Bjånes, A.; De La Fuente, R.; Mena, P. A deep learning ensemble model for wildfire susceptibility mapping. *Ecol. Inform.* **2021**, *65*, 101397. [CrossRef]
54. Bui, D.T.; Bui, Q.-T.; Nguyen, Q.-P.; Pradhan, B.; Nampak, H.; Trinh, P.T. A hybrid artificial intelligence approach using GIS-based neural-fuzzy inference system and particle swarm optimization for wildfire susceptibility modeling at a tropical area. *Agric. For. Meteorol.* **2017**, *233*, 32–44.
55. Tehrany, M.S.; Jones, S.; Shabani, F.; Martínez-Álvarez, F.; Tien Bui, D. A novel ensemble modeling approach for the spatial prediction of tropical wildfire susceptibility using LogitBoost machine learning classifier and multi-source geospatial data. *Theor. Appl. Climatol.* **2019**, *137*, 637–653. [CrossRef]
56. Arpaci, A.; Malowerschnig, B.; Sass, O.; Vacik, H. Using multi variate data mining techniques for estimating fire susceptibility of Tyrolean forests. *Appl. Geogr.* **2014**, *53*, 258–270. [CrossRef]
57. Mitchell, T. *Machine Learning*; McGraw-Hill International: Columbus, OH, USA, 1997.
58. Poole, D.L.; Mackworth, A.K. *Artificial Intelligence: Foundations of Computational Agents*; Cambridge University Press: Cambridge, UK, 2010.
59. Recknagel, F. Applications of machine learning to ecological modelling. *Ecol. Model.* **2001**, *146*, 303–310. [CrossRef]
60. Knudby, A.; LeDrew, E.; Brenning, A. Predictive mapping of reef fish species richness, diversity and biomass in Zanzibar using IKONOS imagery and machine-learning techniques. *Remote Sens. Environ.* **2010**, *114*, 1230–1241. [CrossRef]
61. Chen, W.; Li, H.; Hou, E.; Wang, S.; Wang, G.; Panahi, M.; Li, T.; Peng, T.; Guo, C.; Niu, C. GIS-based groundwater potential analysis using novel ensemble weights-of-evidence with logistic regression and functional tree models. *Sci. Total Environ.* **2018**, *634*, 853–867. [CrossRef]
62. Chen, W.; Yan, X.; Zhao, Z.; Hong, H.; Bui, D.T.; Pradhan, B. Spatial prediction of landslide susceptibility using data mining-based kernel logistic regression, naive Bayes and RBFNetwork models for the Long County area (China). *Bull. Eng. Geol. Environ.* **2019**, *78*, 247–266. [CrossRef]
63. Pham, B.T.; Luu, C.; Van Phong, T.; Trinh, P.T.; Shirzadi, A.; Renoud, S.; Asadi, S.; Van Le, H.; von Meding, J.; Clague, J.J. Can deep learning algorithms outperform benchmark machine learning algorithms in flood susceptibility modeling? *J. Hydrol.* **2021**, *592*, 125615. [CrossRef]
64. Yang, J.; Xu, J.; Zhang, X.; Wu, C.; Lin, T.; Ying, Y. Deep learning for vibrational spectral analysis: Recent progress and a practical guide. *Anal. Chim. Acta* **2019**, *1081*, 6–17. [CrossRef]
65. Shen, D.; Wu, G.; Suk, H.-I. Deep learning in medical image analysis. *Annu. Rev. Biomed. Eng.* **2017**, *19*, 221–248. [CrossRef]
66. LeCun, Y.; Bengio, Y.; Hinton, G. Deep learning. *Nature* **2015**, *521*, 436–444. [CrossRef]
67. Hinton, G.E.; Salakhutdinov, R.R. Reducing the dimensionality of data with neural networks. *Science* **2006**, *313*, 504–507. [CrossRef] [PubMed]
68. Zaremba, W.; Sutskever, I.; Vinyals, O. Recurrent neural network regularization. *arXiv* **2014**, arXiv:1409.2329.
69. Du, Y.; Wang, W.; Wang, L. Hierarchical recurrent neural network for skeleton based action recognition. In Proceedings of the IEEE Conference on Computer Vision and Pattern Recognition, Boston, MA, USA, 7–12 June 2015; pp. 1110–1118.
70. Khan, S.; Yairi, T. A review on the application of deep learning in system health management. *Mech. Syst. Signal Process.* **2018**, *107*, 241–265. [CrossRef]
71. Sauter, T.; Weitzenkamp, B.; Schneider, C. Spatio-temporal prediction of snow cover in the Black Forest mountain range using remote sensing and a recurrent neural network. *Int. J. Climatol.* **2010**, *30*, 2330–2341. [CrossRef]
72. Muhammad, K.; Ahmad, J.; Baik, S.W. Early fire detection using convolutional neural networks during surveillance for effective disaster management. *Neurocomputing* **2018**, *288*, 30–42. [CrossRef]
73. Ham, Y.-G.; Kim, J.-H.; Luo, J.-J. Deep learning for multi-year ENSO forecasts. *Nature* **2019**, *573*, 568–572. [CrossRef] [PubMed]
74. Ngo, P.T.T.; Panahi, M.; Khosravi, K.; Ghorbanzadeh, O.; Kariminejad, N.; Cerda, A.; Lee, S. Evaluation of deep learning algorithms for national scale landslide susceptibility mapping of Iran. *Geosci. Front.* **2021**, *12*, 505–519.
75. Parsaeimehr, E.; Fartash, M.; Torkestani, J.A. An enhanced deep neural network-based architecture for joint extraction of entity mentions and relations. *Int. J. Fuzzy Log. Intell. Syst.* **2020**, *20*, 69–76. [CrossRef]
76. Zhang, G.; Wang, M.; Liu, K. Wildfire susceptibility modeling using a convolutional neural network for Yunnan province of China. *Int. J. Disaster Risk Sci.* **2019**, *10*, 386–403. [CrossRef]
77. Li, X.; Gao, H.; Zhang, M.; Zhang, S.; Gao, Z.; Liu, J.; Sun, S.; Hu, T.; Sun, L. Prediction of Wildfire spread rate using UAV images and an LSTM model considering the interaction between fire and wind. *Remote Sens.* **2021**, *13*, 4325. [CrossRef]
78. Eskandari, S.; Pourghasemi, H.R.; Tiefenbacher, J.P. Relations of land cover, topography, and climate to fire occurrence in natural regions of Iran: Applying new data mining techniques for modeling and mapping fire danger. *For. Ecol. Manag.* **2020**, *473*, 118338. [CrossRef]
79. Otón, G.; Ramo, R.; Lizundia-Loiola, J.; Chuvieco, E. Global detection of long-term (1982–2017) burned area with AVHRR-LTDR data. *Remote Sens.* **2019**, *11*, 2079. [CrossRef]
80. Tran, B.N.; Tanase, M.A.; Bennett, L.T.; Aponte, C. Evaluation of spectral indices for assessing fire severity in Australian temperate forests. *Remote Sens.* **2018**, *10*, 1680. [CrossRef]
81. Miller, J.D.; Knapp, E.E.; Key, C.H.; Skinner, C.N.; Isbell, C.J.; Creasy, R.M.; Sherlock, J.W. Calibration and validation of the relative differenced Normalized Burn Ratio (RdNBR) to three measures of fire severity in the Sierra Nevada and Klamath Mountains, California, USA. *Remote Sens. Environ.* **2009**, *113*, 645–656. [CrossRef]

82. Miller, J.D.; Thode, A.E. Quantifying burn severity in a heterogeneous landscape with a relative version of the delta Normalized Burn Ratio (dNBR). *Remote Sens. Environ.* **2007**, *109*, 66–80. [CrossRef]
83. Gralewicz, N.J.; Nelson, T.A.; Wulder, M.A. Factors influencing national scale wildfire susceptibility in Canada. *For. Ecol. Manag.* **2012**, *265*, 20–29. [CrossRef]
84. Jaafari, A.; Pourghasemi, H.R. Factors influencing regional-scale wildfire probability in Iran: An application of random forest and support vector machine. In *Spatial Modeling in GIS and R for Earth and Environmental Sciences*; Elsevier: Amsterdam, The Netherlands, 2019; pp. 607–619.
85. Moayedi, H.; Mehrabi, M.; Bui, D.T.; Pradhan, B.; Foong, L.K. Fuzzy-metaheuristic ensembles for spatial assessment of wildfire susceptibility. *J. Environ. Manag.* **2020**, *260*, 109867. [CrossRef]
86. Wu, Z.; He, H.S.; Yang, J.; Liang, Y. Defining fire environment zones in the boreal forests of northeastern China. *Sci. Total Environ.* **2015**, *518*, 106–116. [CrossRef] [PubMed]
87. Janiec, P.; Gadal, S. A comparison of two machine learning classification methods for remote sensing predictive modeling of the wildfire in the North-Eastern Siberia. *Remote Sens.* **2020**, *12*, 4157. [CrossRef]
88. Pastor, E.; Zárate, L.; Planas, E.; Arnaldos, J. Mathematical models and calculation systems for the study of wildland fire behaviour. *Prog. Energy Combust. Sci.* **2003**, *29*, 139–153. [CrossRef]
89. Liang, H.; Zhang, M.; Wang, H. A neural network model for wildfire scale prediction using meteorological factors. *IEEE Access* **2019**, *7*, 176746–176755. [CrossRef]
90. Renard, Q.; Pélissier, R.; Ramesh, B.; Kodandapani, N. Environmental susceptibility model for predicting wildfire occurrence in the Western Ghats of India. *Int. J. Wildland Fire* **2012**, *21*, 368–379. [CrossRef]
91. Viedma, O.; Urbieta, I.; Moreno, J.M. Wildfires and the role of their drivers are changing over time in a large rural area of west-central Spain. *Sci. Rep.* **2018**, *8*, 17797. [CrossRef]
92. Bui, D.T.; Hoang, N.-D.; Samui, P. Spatial pattern analysis and prediction of wildfire using new machine learning approach of Multivariate Adaptive Regression Splines and Differential Flower Pollination optimization: A case study at Lao Cai province (Viet Nam). *J. Environ. Manag.* **2019**, *237*, 476–487.
93. Huang, S.; Tang, L.; Hupy, J.P.; Wang, Y.; Shao, G. A commentary review on the use of normalized difference vegetation index (NDVI) in the era of popular remote sensing. *J. For. Res.* **2021**, *32*, 1–6. [CrossRef]
94. Kalantar, B.; Ueda, N.; Idrees, M.O.; Janizadeh, S.; Ahmadi, K.; Shabani, F. Wildfire susceptibility prediction based on machine learning models with resampling algorithms on remote sensing data. *Remote Sens.* **2020**, *12*, 3682. [CrossRef]
95. Mann, M.L.; Batllori, E.; Moritz, M.A.; Waller, E.K.; Berck, P.; Flint, A.L.; Flint, L.E.; Dolfi, E. Incorporating anthropogenic influences into fire probability models: Effects of human activity and climate change on fire activity in California. *PLoS ONE* **2016**, *11*, e0153589. [CrossRef] [PubMed]
96. Benson, R.P.; Roads, J.O.; Weise, D.R. Climatic and weather factors affecting fire occurrence and behavior. *Dev. Environ. Sci.* **2008**, *8*, 37–59.
97. Leuenberger, M.; Parente, J.; Tonini, M.; Pereira, M.G.; Kanevski, M. Wildfire susceptibility mapping: Deterministic vs. stochastic approaches. *Environ. Model. Softw.* **2018**, *101*, 194–203. [CrossRef]
98. Kane, V.R.; Cansler, C.A.; Povak, N.A.; Kane, J.T.; McGaughey, R.J.; Lutz, J.A.; Churchill, D.J.; North, M.P. Mixed severity fire effects within the Rim fire: Relative importance of local climate, fire weather, topography, and forest structure. *For. Ecol. Manag.* **2015**, *358*, 62–79. [CrossRef]
99. Parisien, M.-A.; Snetsinger, S.; Greenberg, J.A.; Nelson, C.R.; Schoennagel, T.; Dobrowski, S.Z.; Moritz, M.A. Spatial variability in wildfire probability across the western United States. *Int. J. Wildland Fire* **2012**, *21*, 313–327. [CrossRef]
100. Thach, N.N.; Ngo, D.B.-T.; Xuan-Canh, P.; Hong-Thi, N.; Thi, B.H.; Nhat-Duc, H.; Dieu, T.B. Spatial pattern assessment of tropical wildfire danger at Thuan Chau area (Vietnam) using GIS-based advanced machine learning algorithms: A comparative study. *Ecol. Inform.* **2018**, *46*, 74–85. [CrossRef]
101. Syphard, A.D.; Radeloff, V.C.; Keuler, N.S.; Taylor, R.S.; Hawbaker, T.J.; Stewart, S.I.; Clayton, M.K. Predicting spatial patterns of fire on a southern California landscape. *Int. J. Wildland Fire* **2008**, *17*, 602–613. [CrossRef]
102. Ghorbanzadeh, O.; Blaschke, T. Wildfire susceptibility evaluation by integrating an analytical network process approach into GIS-based analyses. In Proceedings of the ISERD International Conference, Chicago, IL, USA, 22 August 2018.
103. Al-Fugara, A.k.; Mabdeh, A.N.; Ahmadlou, M.; Pourghasemi, H.R.; Al-Adamat, R.; Pradhan, B.; Al-Shabeeb, A.R. Wildland fire susceptibility mapping using support vector regression and adaptive neuro-fuzzy inference system-based whale optimization algorithm and simulated annealing. *ISPRS Int. J. Geo-Inf.* **2021**, *10*, 382. [CrossRef]
104. Prasad, V.K.; Badarinath, K.; Eaturu, A. Biophysical and anthropogenic controls of wildfires in the Deccan Plateau, India. *J. Environ. Manag.* **2008**, *86*, 1–13. [CrossRef]
105. Setiawan, I.; Mahmud, A.; Mansor, S.; Mohamed Shariff, A.; Nuruddin, A. GIS-grid-based and multi-criteria analysis for identifying and mapping peat swamp wildfire hazard in Pahang, Malaysia. *Disaster Prev. Manag. Int. J.* **2004**, *13*, 379–386. [CrossRef]
106. Farr, T.G.; Rosen, P.A.; Caro, E.; Crippen, R.; Duren, R.; Hensley, S.; Kobrick, M.; Paller, M.; Rodriguez, E.; Roth, L. The shuttle radar topography mission. *Rev. Geophys.* **2007**, *45*, RG2004. [CrossRef]
107. Chuvieco, E.; Congalton, R.G. Application of remote sensing and geographic information systems to wildfire hazard mapping. *Remote Sens. Environ.* **1989**, *29*, 147–159. [CrossRef]

108. Chang, Y.; Zhu, Z.; Bu, R.; Chen, H.; Feng, Y.; Li, Y.; Hu, Y.; Wang, Z. Predicting fire occurrence patterns with logistic regression in Heilongjiang Province, China. *Landsc. Ecol.* **2013**, *28*, 1989–2004. [CrossRef]
109. Dimitrakopoulos, A.; Papaioannou, K.K. Flammability assessment of Mediterranean forest fuels. *Fire Technol.* **2001**, *37*, 143–152. [CrossRef]
110. Van Bellen, S.; Garneau, M.; Bergeron, Y. Impact of climate change on wildfire severity and consequences for carbon stocks in boreal forest stands of Quebec, Canada: A synthesis. *Fire Ecol.* **2010**, *6*, 16–44. [CrossRef]
111. Eskandari, S.; Ghadikolaei, J.O.; Jalilvand, H.; Saradjian, M.R. Prediction of Future Wildfires Using the MCDM Method. *Pol. J. Environ. Stud.* **2015**, *24*, 2309–2314.
112. Martínez, J.; Vega-Garcia, C.; Chuvieco, E. Human-caused wildfire risk rating for prevention planning in Spain. *J. Environ. Manag.* **2009**, *90*, 1241–1252. [CrossRef]
113. Wang, S.; Zhang, K.; Chao, L.; Li, D.; Tian, X.; Bao, H.; Chen, G.; Xia, Y. Exploring the utility of radar and satellite-sensed precipitation and their dynamic bias correction for integrated prediction of flood and landslide hazards. *J. Hydrol.* **2021**, *603*, 126964. [CrossRef]
114. Kanga, S.; Tripathi, G.; Singh, S.K. Wildfire hazards vulnerability and risk assessment in Bhajji forest range of Himachal Pradesh (India): A geospatial approach. *J. Remote Sens. GIS* **2017**, *8*, 25–40.
115. Jolly, W. *Assessing the Impacts of Recent Climate Change on Global Fire Danger*; USDA Forest Service, Rocky Mountain Research Station: Fort Collins, CO, USA, 2014.
116. Field, R.; Spessa, A.; Aziz, N.; Camia, A.; Cantin, A.; Carr, R.; De Groot, W.; Dowdy, A.; Flannigan, M.; Manomaiphiboon, K. Development of a global fire weather database. *Nat. Hazards Earth Syst. Sci.* **2015**, *15*, 1407–1423. [CrossRef]
117. Zhou, T.; Ji, J.; Jiang, Y.; Ding, L. EnKF-Based Real-Time Prediction of Wildfire Propagation. In Proceedings of the 11th Asia-Oceania Symposium on Fire Science and Technology, Taipei, Taiwan, 22–24 October 2020; pp. 713–724.
118. Rodrigues, M.; De la Riva, J. An insight into machine-learning algorithms to model human-caused wildfire occurrence. *Environ. Model. Softw.* **2014**, *57*, 192–201. [CrossRef]
119. Vilar, L.; Woolford, D.G.; Martell, D.L.; Martín, M.P. A model for predicting human-caused wildfire occurrence in the region of Madrid, Spain. *Int. J. Wildland Fire* **2010**, *19*, 325–337. [CrossRef]
120. Rodrigues, M.; Jiménez-Ruano, A.; Peña-Angulo, D.; De la Riva, J. A comprehensive spatial-temporal analysis of driving factors of human-caused wildfires in Spain using Geographically Weighted Logistic Regression. *J. Environ. Manag.* **2018**, *225*, 177–192. [CrossRef] [PubMed]
121. Parisien, M.-A.; Miller, C.; Parks, S.A.; DeLancey, E.R.; Robinne, F.-N.; Flannigan, M.D. The spatially varying influence of humans on fire probability in North America. *Environ. Res. Lett.* **2016**, *11*, 075005. [CrossRef]
122. Nguyen, Q.-H.; Chou, T.-Y.; Yeh, M.-L.; Hoang, T.-V.; Nguyen, H.-D.; Bui, Q.-T. Henry's gas solubility optimization algorithm in formulating deep neural network for landslide susceptibility assessment in mountainous areas. *Environ. Earth Sci.* **2021**, *80*, 414. [CrossRef]
123. Ghorbanzadeh, O.; Blaschke, T.; Gholamnia, K.; Aryal, J. Wildfire susceptibility and risk mapping using social/infrastructural vulnerability and environmental variables. *Fire* **2019**, *2*, 50. [CrossRef]
124. González, M.; Sapiains, R.; Gómez-González, S.; Garreaud, R.; Miranda, A.; Galleguillos, M.; Jacques, M.; Pauchard, A.; Hoyos, J.; Cordero, L. Incendios forestales en Chile: Causas, impactos y resiliencia. *Cent. Cienc. Clima Resiliencia (CR)* **2020**, *2*, 84.
125. Satir, O.; Berberoglu, S.; Donmez, C. Mapping regional wildfire probability using artificial neural network model in a Mediterranean forest ecosystem. *Geomat. Nat. Hazards Risk* **2016**, *7*, 1645–1658. [CrossRef]
126. Jaafari, A. LiDAR-supported prediction of slope failures using an integrated ensemble weights-of-evidence and analytical hierarchy process. *Environ. Earth Sci.* **2018**, *77*, 42. [CrossRef]
127. Tien Bui, D.; Le, K.-T.T.; Nguyen, V.C.; Le, H.D.; Revhaug, I. Tropical wildfire susceptibility mapping at the Cat Ba National Park Area, Hai Phong City, Vietnam, using GIS-based kernel logistic regression. *Remote Sens.* **2016**, *8*, 347. [CrossRef]
128. Hong, H.; Jaafari, A.; Zenner, E.K. Predicting spatial patterns of wildfire susceptibility in the Huichang County, China: An integrated model to analysis of landscape indicators. *Ecol. Indic.* **2019**, *101*, 878–891. [CrossRef]
129. Goodfellow, I.; Bengio, Y.; Courville, A. *Deep Learning*; MIT Press: Cambridge, MA, USA, 2016.
130. Mou, L.; Ghamisi, P.; Zhu, X.X. Deep recurrent neural networks for hyperspectral image classification. *IEEE Trans. Geosci. Remote Sens.* **2017**, *55*, 3639–3655. [CrossRef]
131. Mezaal, M.R.; Pradhan, B.; Sameen, M.I.; Mohd Shafri, H.Z.; Yusoff, Z.M. Optimized neural architecture for automatic landslide detection from high-resolution airborne laser scanning data. *Appl. Sci.* **2017**, *7*, 730. [CrossRef]
132. Mutlu, B.; Nefeslioglu, H.A.; Sezer, E.A.; Akcayol, M.A.; Gokceoglu, C. An experimental research on the use of recurrent neural networks in landslide susceptibility mapping. *ISPRS Int. J. Geo-Inf.* **2019**, *8*, 578. [CrossRef]
133. Abiodun, O.I.; Jantan, A.; Omolara, A.E.; Dada, K.V.; Mohamed, N.A.; Arshad, H. State-of-the-art in artificial neural network applications: A survey. *Heliyon* **2018**, *4*, e00938. [CrossRef]
134. Tealab, A. Time series forecasting using artificial neural networks methodologies: A systematic review. *Future Comput. Inform. J.* **2018**, *3*, 334–340. [CrossRef]
135. Nguyen, H.; Nguyen, Q.-H.; Du, Q.; Ha Thanh, N.; Nguyen, G.; Bui, Q.-T. A novel combination of deep neural network and manta ray foraging optimization for flood susceptibility mapping in Quang Ngai province, Vietnam. *Geocarto Int.* **2021**, *37*, 7531–7555. [CrossRef]

136. Yin, W.; Kann, K.; Yu, M.; Schütze, H. Comparative study of CNN and RNN for natural language processing. *arXiv* **2017**, arXiv:1702.01923.
137. Nguyen, H.D. Hybrid models based on deep learning neural network and optimization algorithms for the spatial prediction of tropical wildfire susceptibility in Nghe An province, Vietnam. *Geocarto Int.* **2022**, *37*, 11281–11305. [CrossRef]
138. Xu, S.; Niu, R. Displacement prediction of Baijiabao landslide based on empirical mode decomposition and long short-term memory neural network in Three Gorges area, China. *Comput. Geosci.* **2018**, *111*, 87–96. [CrossRef]
139. Pascanu, R.; Gulcehre, C.; Cho, K.; Bengio, Y. How to construct deep recurrent neural networks. *arXiv* **2013**, arXiv:1312.6026.
140. Matrenin, P.V.; Manusov, V.Z.; Khalyasmaa, A.I.; Antonenkov, D.V.; Eroshenko, S.A.; Butusov, D.N. Improving accuracy and generalization performance of small-size recurrent neural networks applied to short-term load forecasting. *Mathematics* **2020**, *8*, 2169. [CrossRef]
141. Benzekri, W.; El Moussati, A.; Moussaoui, O.; Berrajaa, M. Early wildfire detection system using wireless sensor network and deep learning. *Int. J. Adv. Comput. Sci. Appl.* **2020**, *11*, 496.
142. Izakian, H.; Pedrycz, W.; Jamal, I. Fuzzy clustering of time series data using dynamic time warping distance. *Eng. Appl. Artif. Intell.* **2015**, *39*, 235–244. [CrossRef]
143. Redmon, J.; Divvala, S.; Girshick, R.; Farhadi, A. You only look once: Unified, real-time object detection. In Proceedings of the IEEE Conference on Computer Vision and Pattern Recognition, Las Vegas, NV, USA, 27–30 June 2016; pp. 779–788.
144. Graves, A.; Mohamed, A.-r.; Hinton, G. Speech recognition with deep recurrent neural networks. In Proceedings of the 2013 IEEE International Conference on Acoustics, Speech and Signal Processing, Vancouver, BC, Canada, 26–31 May 2013; pp. 6645–6649.
145. Wei, D.; Wang, B.; Lin, G.; Liu, D.; Dong, Z.; Liu, H.; Liu, Y. Research on unstructured text data mining and fault classification based on RNN-LSTM with malfunction inspection report. *Energies* **2017**, *10*, 406. [CrossRef]
146. Pomerat, J.; Segev, A.; Datta, R. On neural network activation functions and optimizers in relation to polynomial regression. In Proceedings of the 2019 IEEE International Conference on Big Data (Big Data), Los Angeles, CA, USA, 9–12 December 2019; pp. 6183–6185.
147. Farahani, M.; Razavi-Termeh, S.V.; Sadeghi-Niaraki, A. A spatially based machine learning algorithm for potential mapping of the hearing senses in an urban environment. *Sustain. Cities Soc.* **2022**, *80*, 103675. [CrossRef]
148. Li, Y.-F.; Xie, M.; Goh, T.-N. Adaptive ridge regression system for software cost estimating on multi-collinear datasets. *J. Syst. Softw.* **2010**, *83*, 2332–2343. [CrossRef]
149. Bui, D.T.; Pradhan, B.; Nampak, H.; Bui, Q.-T.; Tran, Q.-A.; Nguyen, Q.-P. Hybrid artificial intelligence approach based on neural fuzzy inference model and metaheuristic optimization for flood susceptibilitgy modeling in a high-frequency tropical cyclone area using GIS. *J. Hydrol.* **2016**, *540*, 317–330.
150. Razavi-Termeh, S.V.; Sadeghi-Niaraki, A.; Choi, S.-M. Spatial modeling of asthma-prone areas using remote sensing and ensemble machine learning algorithms. *Remote Sens.* **2021**, *13*, 3222. [CrossRef]
151. Shabanpour, N.; Razavi-Termeh, S.V.; Sadeghi-Niaraki, A.; Choi, S.-M.; Abuhmed, T. Integration of machine learning algorithms and GIS-based approaches to cutaneous leishmaniasis prevalence risk mapping. *Int. J. Appl. Earth Obs. Geoinf.* **2022**, *112*, 102854. [CrossRef]
152. Ho, T.K.; Hull, J.J.; Srihari, S.N. Decision combination in multiple classifier systems. *IEEE Trans. Pattern Anal. Mach. Intell.* **1994**, *16*, 66–75.
153. Breiman, L. Random forests. *Mach. Learn.* **2001**, *45*, 5–32. [CrossRef]
154. Lawrence, R.L.; Wood, S.D.; Sheley, R.L. Mapping invasive plants using hyperspectral imagery and Breiman Cutler classifications (RandomForest). *Remote Sens. Environ.* **2006**, *100*, 356–362. [CrossRef]
155. Cutler, D.R.; Edwards Jr, T.C.; Beard, K.H.; Cutler, A.; Hess, K.T.; Gibson, J.; Lawler, J.J. Random forests for classification in ecology. *Ecology* **2007**, *88*, 2783–2792. [CrossRef] [PubMed]
156. Razavi-Termeh, S.V.; Sadeghi-Niaraki, A.; Farhangi, F.; Choi, S.-M. Covid-19 risk mapping with considering socio-economic criteria using machine learning algorithms. *Int. J. Environ. Res. Public Health* **2021**, *18*, 9657. [CrossRef]
157. Stumpf, A.; Kerle, N. Object-oriented mapping of landslides using Random Forests. *Remote Sens. Environ.* **2011**, *115*, 2564–2577. [CrossRef]
158. Pourghasemi, H.R.; Gayen, A.; Edalat, M.; Zarafshar, M.; Tiefenbacher, J.P. Is multi-hazard mapping effective in assessing natural hazards and integrated watershed management? *Geosci. Front.* **2020**, *11*, 1203–1217. [CrossRef]
159. Razavi-Termeh, S.V.; Sadeghi-Niaraki, A.; Seo, M.; Choi, S.-M. Application of genetic algorithm in optimization parallel ensemble-based machine learning algorithms to flood susceptibility mapping using radar satellite imagery. *Sci. Total Environ.* **2023**, *873*, 162285. [CrossRef]
160. Kausar, N.; Majid, A. Random forest-based scheme using feature and decision levels information for multi-focus image fusion. *Pattern Anal. Appl.* **2016**, *19*, 221–236. [CrossRef]
161. Farahani, M.; Razavi-Termeh, S.V.; Sadeghi-Niaraki, A.; Choi, S.-M. People's olfactory perception potential mapping using a machine learning algorithm: A Spatio-temporal approach. *Sustain. Cities Soc.* **2023**, *93*, 104472. [CrossRef]
162. Masroor, M.; Razavi-Termeh, S.V.; Rahaman, M.H.; Choudhari, P.; Kulimushi, L.C.; Sajjad, H. Adaptive neuro fuzzy inference system (ANFIS) machine learning algorithm for assessing environmental and socio-economic vulnerability to drought: A study in Godavari middle sub-basin, India. *Stoch. Environ. Res. Risk Assess.* **2023**, *37*, 233–259. [CrossRef]

163. Pourghasemi, H.R.; Gayen, A.; Panahi, M.; Rezaie, F.; Blaschke, T. Multi-hazard probability assessment and mapping in Iran. *Sci. Total Environ.* **2019**, *692*, 556–571. [CrossRef] [PubMed]
164. Kuhn, M.; Johnson, K. *Applied Predictive Modeling*; Springer: Berlin/Heidelberg, Germany, 2013; Volume 26.
165. Dargan, S.; Kumar, M.; Ayyagari, M.R.; Kumar, G. A survey of deep learning and its applications: A new paradigm to machine learning. *Arch. Comput. Methods Eng.* **2020**, *27*, 1071–1092. [CrossRef]
166. Alzubaidi, L.; Zhang, J.; Humaidi, A.J.; Al-Dujaili, A.; Duan, Y.; Al-Shamma, O.; Santamaría, J.; Fadhel, M.A.; Al-Amidie, M.; Farhan, L. Review of deep learning: Concepts, CNN architectures, challenges, applications, future directions. *J. Big Data* **2021**, *8*, 53. [CrossRef]
167. Zhou, Y.; Li, Y.; Wang, D.; Liu, Y. A multi-step ahead global solar radiation prediction method using an attention-based transformer model with an interpretable mechanism. *Int. J. Hydrogen Energy* **2023**, *48*, 15317–15330. [CrossRef]
168. Wei, Y.; Wang, W.; Tang, X.; Li, H.; Hu, H.; Wang, X. Classification of alpine grasslands in cold and high altitudes based on multispectral Landsat-8 images: A case study in Sanjiangyuan National Park, China. *Remote Sens.* **2022**, *14*, 3714. [CrossRef]
169. Zhan, J.; Hu, Y.; Cai, W.; Zhou, G.; Li, L. PDAM–STPNNet: A small target detection approach for wildland fire smoke through remote sensing images. *Symmetry* **2021**, *13*, 2260. [CrossRef]
170. Zheng, S.; Gao, P.; Wang, W.; Zou, X. A Highly Accurate Wildfire Prediction Model Based on an Improved Dynamic Convolutional Neural Network. *Appl. Sci.* **2022**, *12*, 6721. [CrossRef]
171. Lin, X.; Li, Z.; Chen, W.; Sun, X.; Gao, D. Wildfire Prediction Based on Long-and Short-Term Time-Series Network. *Forests* **2023**, *14*, 778. [CrossRef]
172. Li, Z.; Huang, Y.; Li, X.; Xu, L. Wildland fire burned areas prediction using long short-term memory neural network with attention mechanism. *Fire Technol.* **2021**, *57*, 1–23. [CrossRef]
173. Choi, M.-Y.; Jun, S. Fire risk assessment models using statistical machine learning and optimized risk indexing. *Appl. Sci.* **2020**, *10*, 4199. [CrossRef]
174. Ghorbanzadeh, O.; Valizadeh Kamran, K.; Blaschke, T.; Aryal, J.; Naboureh, A.; Einali, J.; Bian, J. Spatial prediction of wildfire susceptibility using field survey gps data and machine learning approaches. *Fire* **2019**, *2*, 43. [CrossRef]
175. Yousefi, S.; Pourghasemi, H.R.; Emami, S.N.; Pouyan, S.; Eskandari, S.; Tiefenbacher, J.P. A machine learning framework for multi-hazards modeling and mapping in a mountainous area. *Sci. Rep.* **2020**, *10*, 12144. [CrossRef]
176. Razavi-Termeh, S.V.; Sadeghi-Niaraki, A.; Choi, S.-M. Ubiquitous GIS-based wildfire susceptibility mapping using artificial intelligence methods. *Remote Sens.* **2020**, *12*, 1689. [CrossRef]
177. Eskandari, S.; Pourghasemi, H.R.; Tiefenbacher, J.P. Fire-susceptibility mapping in the natural areas of Iran using new and ensemble data-mining models. *Environ. Sci. Pollut. Res.* **2021**, *28*, 47395–47406. [CrossRef]
178. Mohajane, M.; Costache, R.; Karimi, F.; Pham, Q.B.; Essahlaoui, A.; Nguyen, H.; Laneve, G.; Oudija, F. Application of remote sensing and machine learning algorithms for wildfire mapping in a Mediterranean area. *Ecol. Indic.* **2021**, *129*, 107869. [CrossRef]
179. Flannigan, M.D.; Stocks, B.J.; Wotton, B.M. Climate change and wildfires. *Sci. Total Environ.* **2000**, *262*, 221–229. [CrossRef] [PubMed]
180. Hantson, S.; Andela, N.; Goulden, M.L.; Randerson, J.T. Human-ignited fires result in more extreme fire behavior and eco-system impacts. *Nat. Commun.* **2022**, *13*, 2717. [CrossRef] [PubMed]
181. Jin, R.; Lee, K.-S. Investigation of Wildfire Characteristics in North Korea Using Remote Sensing Data and GIS. *Remote Sens.* **2022**, *14*, 5836. [CrossRef]
182. Naderpour, M.; Rizeei, H.M.; Ramezani, F. Wildfire risk prediction: A spatial deep neural network-based framework. *Remote Sens.* **2021**, *13*, 2513. [CrossRef]